National Technical University of Athens

School of Naval Architecture and Marine Engineering

Shipbuilding Technology Laboratory

Thesis

Detailed Finite Element modeling of sandwich material coupons used for core characterization in shear

NTOUNI KATERINA

SUPERVISOR: Assistant Professor K. ANYFANTIS

October 2020, Athens

Acknowledgements

I would like to thank my supervisor Mr. Anyfantis for his invaluable advice and all the guidance that he provided me during the realization of this thesis.

Moreover, I would like to express my thanks to my family and my close friends for their support during all this time.

Abstract

The subject thesis had as scope the finite element modeling of sandwich material specimens, used in tests conducted for the characterizations of the shear properties of the core, in order to investigate which are the phenomena that occur during their loading.

Models for 3-point bending and shear stress-calculation tests were developed in Abaqus based on the testing standards ISO 14125 and ASTM C273 and the materials were modeled, so as to obtain a response similar to the one observed through the actual experiments.

The main material properties and the geometry of the model where obtained by previous research on this topic and were used as a starting point in order to model all the linear elastic and damage properties of the materials.

Various modeling techniques, such as modeling of the damage response and cohesive zone modeling were introduced in an effort to capture the response of the specimens during the test.

Περίληψη

Στην παρούσα διπλωματική έγινε μοντελοποίηση δοκιμίων από sandwich υλικά, τα οποία χρησιμοποιήθηκαν σε μηχανικές δοκιμές για την εύρεση των χαρακτηριστικών διάτμησης του πυρήνα, με σκοπό να βρεθεί ποια είναι τα φαινόμενα που λαμβάνουν χώρα κατά τη φόρτισή τους.

Μοντέλα για κάμψη τριών σημείων και δοκιμές διάτμησης αναπτύχθηκαν στο Abaqus, με βάση τα πειραματικά πρότυπα ISO 14125 και ASTM C273 και τα υλικά των δοκιμίων μοντελοποιήθηκαν έτσι ώστε η απόκριση τους σε φόρτιση να είναι όμοια με αυτή που παρατηρήθηκε στις πειραματικές δοκιμές.

Τα κύρια χαρακτηριστικά του υλικού και η γεωμετρία των μοντέλων λήφθηκαν από προηγούμενη έρευνα στο συγκεκριμένο θέμα και χρησιμοποιήθηκαν ως αρχικό σημείο για την πλήρη μοντελοποίηση των ελαστικών ιδιοτήτων και των χαρακτηριστικών αστοχίας των υλικών.

Διάφορες τεχνικές, όπως μοντελοποίηση της αστοχίας των υλικών και cohesive zone modeling χρησιμοποιήθηκαν στα μοντέλα προκειμένου η απόκρισή τους να είναι όσο πιο κοντά γίνεται σε αυτή που παρατηρήθηκε κατά το πείραμα.

Contents

1.Composite material theory and applications

1.1 Introduction

Composites are materials created from two or more constituent materials with significantly different physical or chemical properties which when combined, result in a material with better characteristics than those of the individual components. The individual components of the composites remain distinct and separate in the finished product, a fact that differentiates composites from mixtures and solutions.

The advanced properties that composites have, such as their high strength in conjunction with their low weight, their great fatigue characteristics and their low cost of repair, have led them to be widely used and one of the most preferable materials for advanced structures.

1.2 Composite material categories

Composite materials can be divided in three main categories, based on the form of the reinforcement, which are fibrous composite materials, particulate composite materials and laminated composite materials.

Fibrous composite materials are composed of the matrix and the reinforcing fibers. Fibers are those reinforcements characterized by a length much larger than their transverse dimensions and are distributed in the matrix with either a specific or a random orientation.

Particulate composite materials consist of particulates of one or more materials randomly distributed within a matrix. Particles may be of any shape or size, but are generally spherical, ellipsoidal, polyhedral, or irregular in shape with their dimensions typically of the order of a few microns.

Laminated composite materials are composed of multiple layers of either different composite materials or the same material in different orientations, permanently bonded together using an adhesive (e.g. the matrix material).

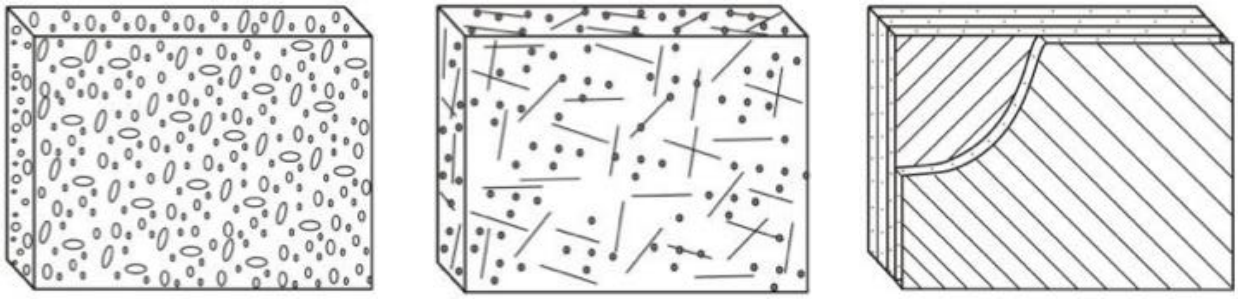

Figure 1.1 Categories of composite materials: particulate composites, fibrous composites and laminated composites

1.3 Composite constituents

The basic constituents of the composite materials are the matrix and the reinforcements, which usually are in the form of fibers. The fibers carry most of the load and provide the stiffness to the material, while the role of the matrix is to support the fibers, to keep them oriented, to protect them from the environment and to transfer the load between the fibers. The vast array of fibers and matrices with different characteristics that are available allow to produce a variety of different composite materials with a wide range of mechanical properties.

Matrices

Matrices can be composed by either organic polymers or inorganic materials. Organic polymers (resins) are divided in two categories, namely thermoplastics and thermosettings. The former soften upon heating and can be reshaped with the impose of heat and pressure, while the latter become cross-linked during the process of polymerism and curing and do not soften with heating. On the other hand, inorganic polymers include metals, ceramics and cement (concrete). Metal and ceramic matrices have a much higher density and better mechanical properties than the polymeric ones and are used in very advanced applications. Carbon for example that comprises a ceramic matrix can be combined with carbon fibers to form composites than can be used in applications where extreme mechanical and thermal loads are present (e.g. in space). For less advanced applications where the temperatures are kept at lower levels, the polymeric matrices that have much lower density are mostly preferred. Since marine applications are included in the aforementioned category and the majority of the currently used composites are made of polymeric matrices, emphasis in this chapter is given on polymeric matrices rather than on the inorganic ones.

The main requirements the resins should meet are high ductility, high toughness, low viscosity, excellent processability, low shrinkage during curing, low moisture absorption and good compatibility with fibers and adhesives [1].

As already mentioned, inorganic polymers consist of two categories, the thermoplastic and the thermosetting resins. Thermoplastic resins, such as polypropylene, polyvinyl chloride (PVC), nylon and polyurethane, exhibit good chemical resistance, good delamination resistance, low moisture absorption and their processing is faster in comparison to the thermosetting resins, since no curing reaction is required, however their cost is higher. Thermosetting resins or else called thermosets are the ones more widely used in marine applications and include the polyester, vinylester, epoxy, polyimides and phenolic resins.

- Polyester resins

Polyester resins are the most common type of resin used in marine structures and are divided into orthophalic and isophalic polyesters. The first type is cheaper and the most widespread in the construction of small boats, while the second one is more expensive, has better water resistance and is used in more advanced marine structures [20]. Overall, polyester resins have good heat resistance and electrical properties, low viscosity, excellent mechanical performance when cured at room temperature and low cost, however, they are sensitive to UV radiation, tend to degrade over time and show a large volumetric shrinkage, that leads to residual stresses in the composites. Polyester resins are mainly used in infusion manufacturing and for the hand lay-up method, particularly for composites with glass fibers [1].

- Vinylester resins

Vinylester resins are fabricated from epoxy resins, have lower viscosity than polyester, almost the same cost, and show better resistance to chemicals and water and better fatigue properties.

- Epoxy resins

Epoxy resins have better mechanical properties than the polyester ones, they possess high strength and flexibility, higher resistance to chemical and solvents, low shrinkage during curing and better adhesion with the reinforcing fibers. They can be used with many different types of fibers (glass, carbon, aramid etc), they are widely used as adhesives and they require the use of a hardener during their curing

process. The disadvantages of epoxy resins are their high cost, their high thermal coefficient of expansion and the fact that they cannot be used in temperatures above 175˚C.

- Phenolic resins

Phenolic resins are heat resistant resins which can maintain their mechanical properties up to high temperatures, they have low viscosity and low cost, however, they have a much higher moisture absorption level when compared to polyester resins.

- Polyimides

Similarly to the phenolic resins, polyimide resins possess great heat and fire resistance properties, making them suitable for high temperature applications, as well as high mechanical strength and good chemical resistance properties. However, they are difficult to process and they are more brittle in comparison to other resins.

- Polyurethane

Polyurethane is a thermoset resin with excellent mechanical properties, it gives strong adhesive bonds and can be used in a wide range of applications.

- Shape memory polymer (SPM) resins

Another type of resin that is, however, used in very advanced applications is the shape memory polymer resin. This type of resins, when heated above their glass transition temperature (Tg), become flexible and elastic allowing their easy configuration. Their shape is formed at this state and once they are cooled again, the new shape is maintained. SPM resins can be shaped and reshaped multiple times without losing their material properties.

Fibers

Fibers are generally able to withstand only tensile loads on their own, however, when imbedded in resin to form a composite material, they become able to also carry compressive, bending and shear loads, providing most of the composite material’s stiffness.

- Glass fibers

This type of fiber is the most used type of reinforcement in large low-cost structures such as vessels, civil engineering structures and wind turbine blades, mainly due to its good mechanical properties (e.g. high tensile strength) and low cost. E-glass fibers are the ones used in the majority of GFPR applications, have low cost and great electrical insulation properties, while other more expensive types such as S and E-CR fibers are stronger and more corrosion resistant.

Glass fibers are produced as very small diameter filaments, with their diameter ranging usually from 3 to 20 μm and are combined in twisted or untwisted bundles of filaments called yarns and rovings respectively [2]. Yarns and rovings can be further combined to create a variety of two-dimensional architectures, the most common of which are woven rovings (WR), unidirectional rovings (UD) and woven fabrics or be used to create chopped strand mats (CSM). Chopped strand mat consists of short length randomly laid fibers produced by chopping continuous strand rovings into short lengths, and a binder which holds the cut fibers together. Woven rovings are created by rovings being woven in two mutually perpendicular directions, while woven fabrics are created by weaving yarns, resulting in lighter and more expensive fabrics than the previous ones. Rovings can also be arranged parallel to each other and be sewn or bonded together with a binder, creating this way unidirectional rovings.

- Carbon/Graphite fibers

This type of fibers has superior mechanical strength in comparison to glass fibers, however, they are much more expensive. Based on their production method, different types of carbon/graphite fibers can be produced with a great variety of elastic moduli and mechanical strength, varying from 200 to 830 GPa and 1500 to 4500 MPa respectively. Carbon fibers contain 80-95 percent carbon while graphite fibers are composed of at least 99 percent carbon [20].

Carbon fibers can be found in various forms, such as yarns, untwisted bundles of parallel filaments, called tows (similar to the rovings for glass fibers), woven fabrics and mats [2].

- Aramid fibres

Aramid fibers are synthetic polymer fibers (aromatic polyamides) mostly know as Kevlar®(para-arimide) and Nomex®(meta-aramide). Their main characteristics are their low density and high tensile strength, resulting in a very high specific strength. They also show a good resistance to abrasion and organic solvents, have great heat and flame resistance properties and an excellent vibration damping factor.

- Other fibers

In addition to the above mentioned, other types of fibers that can be used as reinforcements for specific applications are boron fibers (larger in size in comparison to glass/carbon and aramid fibers), ceramic (silicon carbide and alumina) and metallic fibers as well as natural fibers (animal, mineral or cellulose fibers).

A comparison of the mechanical properties of typical types of fibers are shown in table 1.1.

Table 1.1. Mechanical properties of typical reinforcing fibers

Fiber/ Wire	Density ρ (kN/m^3)	Tensile Strength S (MPa)	S/ρ (km)	Tensile Modulus (GPa)	E/ρ (Mm)
Aluminum	26.3	620	24	73	2.8
Titanium	46.1	1,930	42	115	2.5
Steel	76.6	4,100	54	207	2.7
E-glass	25.0	3,500	140	72	2.9
S-glass	24.4	4,800	197	86	3.5
Carbon	13.8	1,700	123	186	13.5
Boron	25.2	3,450	137	400	15.9
Graphite	13.8	1,700	123	255	18.5

1.4 Applications of composites

Composites are nowadays used in a great variety of applications. Although emphasis on subject chapter is given on their marine applications, composites are also well known and widely used in other sectors such as aerospace, in military, business and commercial aircrafts of all sizes, including spacecrafts, in the automotive industry in various parts of vehicles as well as in the building and civil engineering sector. They are also used in renewable energy applications such as in wind turbine blades, in the medical sector (e.g. for transplants), for electrical applications, for pipes, tanks, sewage and water treatment systems.

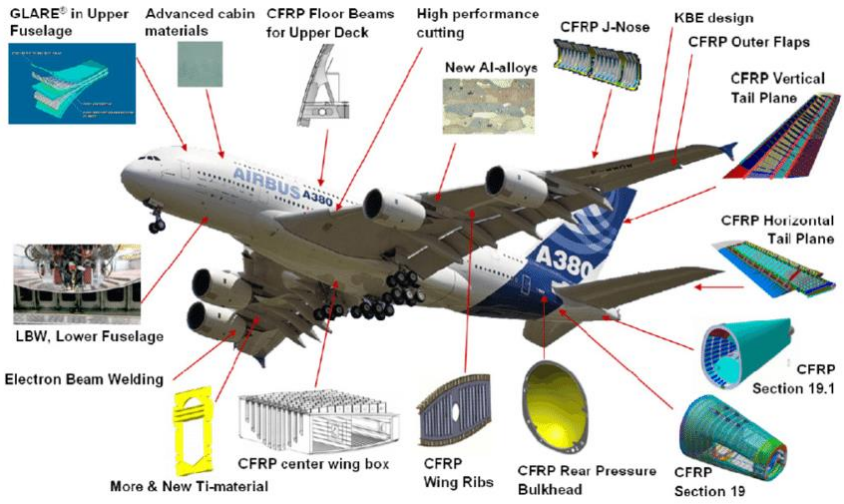

Figure 1.2 Applications of composites in aircrafts

1.4.1 Marine applications of composites

- Small vessels

A wide range of small vessels are fabricated with composite materials, mainly GFRP, including speed boats, life boats, yachts, canoes and kayaks, launch boats, skiffs and small fishing boats. Glass fiber reinforced composites are very popular in the construction of such vessels due to their low maintenance and repair cost and their ability to be tailored in very complex forms. For larger boats, with more than 40 meters length, steel is preferred over composites, due to its lowest cost, apart from certain applications where the composite materials properties, such as low weight and corrosion resistance, are required [20].

- Military vessels

Composite materials are used in many military vessels, with their most important application being in the mine countermeasure vessels (MCMV's). Subject vessels are designed for locating and destroying sea-mines thus the non-magnetic properties of composites materials are essential for this cause [4]. Other applications of composites include patrol boats, corvettes and submarines.

- Superstructures

When used in the constructional parts of vessels' superstructures, composite materials contribute in creating less stiff superstructures which can lead to a decline in the fatigue cracks created in the hull due to interaction between the hull and the superstructures [20]. Apart from the constructional components of the superstructures, other uses of composites can be in doors, hatches, funnels and they can be proven to have better fire resistance in comparison to aluminium which is commonly used.

- Other applications

In addition to those already mentioned, composites can also be used in other marine applications such as in propulsion systems for propellers, propulsion shafts and propulsors, for rudder and radar masts.

Figure 1.3 M80 Stiletto naval ship made of carbon fiber composite

Figure 1.4: Minesweeper made from composite materials.

1.5. Sandwich composites

1.5.1 Introduction

Sandwich composites are a special class of composites created by attaching two thin, strong and stiff skins to a lower density, relatively thick and of lower mechanical strength core. The main advantage of sandwich composites is their high bending stiffness to weight ratio, while some other of their benefits are their high resistance to mechanical fatigue, their good damping characteristics as well as their improved thermal insulation properties [3].

Some of the applications of sandwich composites are in aircrafts, missiles and spacecrafts structures due to the high strength to weight ratio as well as in vessels, where they can be used in various parts, such as for decks and bulkheads.

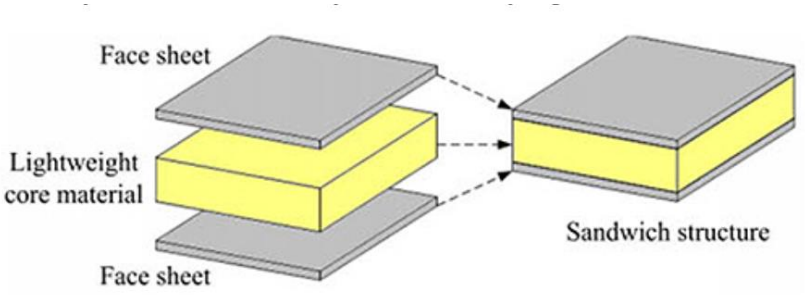

Figure 1.5 : Sandwich materials

1.5.2. Sandwich composites constituents

Sandwich composites are composed by two skins, the core and the adhesive, each of which plays an equally important role in the overall strength of the sandwich structure.

Skins

Skins can be made either from isotropic materials (metals) or from composite laminates and should have small thickness compared to the core. Their role is to carry the tensile and compressive stresses, due to bending loads, as well as to carry the local pressure imposed on them.

Core

On the other hand, the role of the core is to support the skins and to carry the shear and compressive loads. The core has to be light enough, so that the weight of the sandwich is kept low, but at the same time it needs to be stiff and rigid enough, so as to be able to keep the distance between the skins constant as well as withstand the shear stresses.

Adhesive

The adhesive is responsible for keeping the skins and the core bonded, so that stresses can be transferred from the skins to the core. It needs to be compatible with the materials of both skins and core in order to be able to bind them successfully and to have similar or better mechanical properties than these of the core, ensuring that it will not fail prior to the other constituents parts, causing debonding [5].

1.5.3. Core materials

Cores can be made from a great variety of materials ranging from natural materials such as balsa and plywood to synthetic foams and honeycombs.

Foam cores

- PVC foams

Polyvinyl chloride foams (PVC) can have either a cross-linked or a linear form. Cross-linked PVC foams are a mixture of polyvinyl copolymer with stabilizers, plasticizers, cross-linking compounds and blowing agents. They are fabricated by heating their components under pressure, in order for the cross-linking reaction to be initiated and are then submerged into hot water, where they are expanded up to the desired density. PVC foams exhibit a good resistance in water integration and good damping characteristics.

- PET foams

These are thermoplastic foams fabricated by polyethylene terephthalate and possess excellent thermal stability and a high degree of fire resistance.

- PES foams

Subject foams are created from extrusion of thermoplastic polyethersulfine. They have excellent fire resistance properties, improved dielectric properties and a very low level of water absorption.

- PU foams

Polyurethane foams have relatively low shear strength and in general lower mechanical properties in relation to PVC foams of the same density, however they can maintain their mechanical properties up to higher temperatures than PVC. They are extremely flammable and when burned they produce very toxic gases [20].

- PMI foams

Polymethacrylimide (PMI) foam is a closed-cell, high temperature resistance foam, generally used in composite prepreg constructions.

Syntactic foams

Syntactic foams are made by mixing hollow microspheres in resin, making a thick mixture than can be applied by hand or sprayed.

Wooden type cores

Wooden type cores include among others balsa, plywood and redwood. Balsa has a high aspect ratio and directionally aligned cells, such that the grain is oriented in the direction of the maximum stress. It is a very stiff core which, however, exhibits a high level of water absorption and is susceptible to rot.

Honeycombs

Honeycombs cores can be made, among others, from aluminum alloys, phenolic resin impregnated fiberglass and aramid fiber paper and have high specific stiffness and specific compression strength as well very low weight. However, their cost is very high and they are mainly used in the aerospace industry and in applications where a very low weight is requested.

1.6 Mechanics of Composite Materials

1.6.1 Generally anisotropic materials

We consider a rectangular cuboid with dimensions dx, dy, dz, which represents a point particle of the material.

In general, the deformations of the point particle are given by the following equation (1.1)

$$\varepsilon_{ij} = \frac{1}{2}\left(u_{i,j} + u_{j,i} + u_{k,i}\, u_{k,j} \right) \tag{1.1}$$

where u are the relevant displacements in each direction.

Considering small deformations and a linear elastic behavior of the material, the equation (1.1) can be simplified in (1.2).

$$\varepsilon_{ij} = \frac{1}{2}\left(u_{i,j} + u_{j,i} \right) \tag{1.2}$$

In total there are three normal and three shear strains given by the following equations:

$$\begin{aligned} \varepsilon_{xx} = \varepsilon_x = \frac{\partial u}{\partial x} \quad , \quad \varepsilon_{xy} = \frac{1}{2}\left(\frac{\partial u}{\partial y} + \frac{\partial v}{\partial x}\right) = \frac{1}{2}\gamma_{xy} \\ \varepsilon_{yy} = \varepsilon_y = \frac{\partial v}{\partial y} \quad , \quad \varepsilon_{yz} = \frac{1}{2}\left(\frac{\partial v}{\partial z} + \frac{\partial w}{\partial y}\right) = \frac{1}{2}\gamma_{yz} \\ \varepsilon_{zz} = \varepsilon_z = \frac{\partial w}{\partial z} \quad , \quad \varepsilon_{xz} = \frac{1}{2}\left(\frac{\partial u}{\partial z} + \frac{\partial w}{\partial x}\right) = \frac{1}{2}\gamma_{xz} \end{aligned} \tag{1.3}$$

For a generally anisotropic linearly elastic material, the stress-strain relationship in the x,y,z global coordinate system is:

$$\begin{Bmatrix} \sigma_x \\ \sigma_y \\ \sigma_z \\ \tau_{yz} \\ \tau_{xz} \\ \tau_{xy} \end{Bmatrix} = \begin{bmatrix} \bar{C}_{11} & \bar{C}_{12} & \bar{C}_{13} & \bar{C}_{14} & \bar{C}_{15} & \bar{C}_{16} \\ \bar{C}_{12} & \bar{C}_{22} & \bar{C}_{23} & \bar{C}_{24} & \bar{C}_{25} & \bar{C}_{26} \\ \bar{C}_{13} & \bar{C}_{23} & \bar{C}_{33} & \bar{C}_{34} & \bar{C}_{35} & \bar{C}_{36} \\ \bar{C}_{14} & \bar{C}_{24} & \bar{C}_{34} & \bar{C}_{44} & \bar{C}_{45} & \bar{C}_{46} \\ \bar{C}_{15} & \bar{C}_{25} & \bar{C}_{35} & \bar{C}_{45} & \bar{C}_{55} & \bar{C}_{56} \\ \bar{C}_{16} & \bar{C}_{26} & \bar{C}_{36} & \bar{C}_{46} & \bar{C}_{56} & \bar{C}_{66} \end{bmatrix} \begin{Bmatrix} \varepsilon_x \\ \varepsilon_y \\ \varepsilon_z \\ \gamma_{yz} \\ \gamma_{xz} \\ \gamma_{xy} \end{Bmatrix} \tag{1.4}$$

where $\bar{C}_{ij}$ are the elements of the stiffness matrix $[\bar{C}]$ in the x,y,z global coordinate system.

By inversion of the above equation, the strain-stress relationship can be obtained.

$$\begin{Bmatrix} \varepsilon_x \\ \varepsilon_y \\ \varepsilon_z \\ \gamma_{yz} \\ \gamma_{xz} \\ \gamma_{xy} \end{Bmatrix} = \begin{bmatrix} \bar{S}_{11} & \bar{S}_{12} & \bar{S}_{13} & \bar{S}_{14} & \bar{S}_{15} & \bar{S}_{16} \\ \bar{S}_{12} & \bar{S}_{22} & \bar{S}_{23} & \bar{S}_{24} & \bar{S}_{25} & \bar{S}_{26} \\ \bar{S}_{13} & \bar{S}_{23} & \bar{S}_{33} & \bar{S}_{34} & \bar{S}_{35} & \bar{S}_{36} \\ \bar{S}_{14} & \bar{S}_{24} & \bar{S}_{34} & \bar{S}_{44} & \bar{S}_{45} & \bar{S}_{46} \\ \bar{S}_{15} & \bar{S}_{25} & \bar{S}_{35} & \bar{S}_{45} & \bar{S}_{55} & \bar{S}_{56} \\ \bar{S}_{16} & \bar{S}_{26} & \bar{S}_{36} & \bar{S}_{46} & \bar{S}_{56} & \bar{S}_{66} \end{bmatrix} \begin{Bmatrix} \sigma_x \\ \sigma_y \\ \sigma_z \\ \tau_{yz} \\ \tau_{xz} \\ \tau_{xy} \end{Bmatrix} \tag{1.5}$$

where $\bar{S}_{ij}$ are the elements of the compliance matrix $[\bar{S}]$ in the x,y,z global coordinate system.

In the x_1,x_2,x_3 coordinate system the stress-strain and the strain-stress relationships are:

$$\begin{Bmatrix} \sigma_1 \\ \sigma_2 \\ \sigma_3 \\ \tau_{23} \\ \tau_{13} \\ \tau_{12} \end{Bmatrix} = \begin{bmatrix} C_{11} & C_{12} & C_{13} & C_{14} & C_{15} & C_{16} \\ C_{12} & C_{22} & C_{23} & C_{24} & C_{25} & C_{26} \\ C_{13} & C_{23} & C_{33} & C_{34} & C_{35} & C_{36} \\ C_{14} & C_{24} & C_{34} & C_{44} & C_{45} & C_{46} \\ C_{15} & C_{25} & C_{35} & C_{45} & C_{55} & C_{56} \\ C_{16} & C_{26} & C_{36} & C_{46} & C_{56} & C_{66} \end{bmatrix} \begin{Bmatrix} \varepsilon_1 \\ \varepsilon_2 \\ \varepsilon_3 \\ \gamma_{23} \\ \gamma_{13} \\ \gamma_{12} \end{Bmatrix} \tag{1.6}$$

$$\begin{Bmatrix} \varepsilon_1 \\ \varepsilon_2 \\ \varepsilon_3 \\ \gamma_{23} \\ \gamma_{13} \\ \gamma_{12} \end{Bmatrix} = \begin{bmatrix} S_{11} & S_{12} & S_{13} & S_{14} & S_{15} & S_{16} \\ S_{12} & S_{22} & S_{23} & S_{24} & S_{25} & S_{26} \\ S_{13} & S_{23} & S_{33} & S_{34} & S_{35} & S_{36} \\ S_{14} & S_{24} & S_{34} & S_{44} & S_{45} & S_{46} \\ S_{15} & S_{25} & S_{35} & S_{45} & S_{55} & S_{56} \\ S_{16} & S_{26} & S_{36} & S_{46} & S_{56} & S_{66} \end{bmatrix} \begin{Bmatrix} \sigma_1 \\ \sigma_2 \\ \sigma_3 \\ \tau_{23} \\ \tau_{13} \\ \tau_{12} \end{Bmatrix} \tag{1.7}$$

where C_{ij} and $S_{ij}$are the elements of the stiffness and the compliance matrix, respectively, in the x_1, x_2, x_3 coordinate system.

As has already been expressed by the above equations the compliance matrix is the inverse of the stiffness matrix and they are both symmetrical, for elastic materials.

The values of the elements of the compliance matrix can be calculated with the aid of mechanical tests and in the case of an orthotropic material, they are given by the following equations.

$$S_{11} = \frac{1}{E_1} \quad , \quad S_{12} = -\frac{v_{12}}{E_1} = -\frac{v_{21}}{E_2} \quad , \; S_{13} = -\frac{v_{13}}{E_1} = -\frac{v_{31}}{E_3}$$

$$S_{22} = \frac{1}{E_2} \quad , \quad S_{32} = -\frac{v_{23}}{E_2} = -\frac{v_{32}}{E_3} \quad , \quad S_{33} = \frac{1}{E_3} \tag{1.8}$$

$$S_{44} = \frac{1}{G_{23}} \quad , \quad S_{55} = \frac{1}{G_{13}} \quad , \qquad S_{66} = \frac{1}{G_{12}}$$

where

E_1 , E_2 , E_3 are the Young moduli in directions 1,2,3, v_{ij} is the Poisson ratio and G_{13}, G_{23}, G_{12} are the Shear moduli in planes 1-3, 2-3 and 1-2, respectively.

The rest of the compliance matrix elements, for the case of an orthotropic material, are equal to zero.

By inversion of the compliance matrix, the values of the stiffness matrix, for the same material, are as following.

$$\begin{aligned}
C_{11} &= \frac{E_1(1 - v_{23}v_{32})}{\Delta} \ , \qquad C_{12} = \frac{E_1(v_{21} + v_{31}v_{23})}{\Delta} = \frac{E_2(v_{12} + v_{32}v_{13})}{\Delta} \\
C_{22} &= \frac{E_2(1 - v_{31}v_{13})}{\Delta} \ , \qquad C_{13} = \frac{E_1(v_{31} + v_{21}v_{32})}{\Delta} = \frac{E_3(v_{13} + v_{12}v_{23})}{\Delta} \\
C_{33} &= \frac{E_3(1 - v_{21}v_{12})}{\Delta} \ , \qquad C_{23} = \frac{E_2(v_{32} + v_{12}v_{31})}{\Delta} = \frac{E_3(v_{23} + v_{21}v_{13})}{\Delta} \\
C_{44} &= G_{23} \ , \qquad C_{55} = G_{13} \ , \qquad C_{66} = G_{12}
\end{aligned} \tag{1.9}$$

1.6.2. Classical Laminate Theory

The classical laminated plate theory is based on the Kirchhoff hypothesis and ignores the effects of transverse shear deformation, normal stress, normal strain and nonlinear in-plane normal strain distribution through the thickness of the plate. These assumptions are expressed as:

$$\sigma_z = \tau_{yz} = \tau_{zx} = \varepsilon_z = \gamma_{yz} = \gamma_{zx} = 0 \tag{1.10}$$

The strains are given by the following equation:

$$\begin{Bmatrix} \varepsilon_x \\ \varepsilon_y \\ \gamma_{xy} \end{Bmatrix} = \begin{Bmatrix} \varepsilon_{xo} \\ \varepsilon_{yo} \\ \gamma_{xyo} \end{Bmatrix} + z \begin{Bmatrix} k_x \\ k_y \\ k_{xy} \end{Bmatrix} \tag{1.11}$$

where z is the distance from the mid plane, $\varepsilon_{xo}, \varepsilon_{yo}, \gamma_{xyo}$ are the strains in the mid plane and k_x, k_y, k_{xy} are the curvatures of the mid plane, which are calculated by equations (1.12),(1.13).

$$\begin{Bmatrix} \varepsilon_{xo} \\ \varepsilon_{yo} \\ \gamma_{xyo} \end{Bmatrix} = \begin{Bmatrix} \dfrac{\partial u_o}{\partial x} \\ \dfrac{\partial v_o}{\partial y} \\ \dfrac{\partial u_o}{\partial y} + \dfrac{\partial v_o}{\partial x} \end{Bmatrix} \tag{1.12}$$

$$\begin{Bmatrix} k_x \\ k_y \\ k_{xy} \end{Bmatrix} = -\begin{Bmatrix} \dfrac{\partial^2 w_o}{\partial x^2} \\ \dfrac{\partial^2 w_o}{\partial y^2} \\ 2\,\dfrac{\partial^2 w_o}{\partial x\,\partial y} \end{Bmatrix} \tag{1.13}$$

The stresses in each ply are calculated as a function of the strains by equation (1.14):

$$\begin{Bmatrix} \sigma_x \\ \sigma_y \\ \tau_{xy} \end{Bmatrix} = \begin{bmatrix} \bar{Q}_{11} & \bar{Q}_{12} & \bar{Q}_{16} \\ \bar{Q}_{12} & \bar{Q}_{22} & \bar{Q}_{26} \\ \bar{Q}_{16} & \bar{Q}_{26} & \bar{Q}_{66} \end{bmatrix} \begin{Bmatrix} \varepsilon_x \\ \varepsilon_y \\ \gamma_{xy} \end{Bmatrix} \tag{1.14}$$

where $[\bar{Q}]$ is the 2D plane-stress stiffness matrix in the x,y coordinate system.

The in-plane forces and moments on a small element are:

$$\begin{Bmatrix} N_x \\ N_y \\ N_{xy} \end{Bmatrix} = \int_{-t/2}^{t/2} \begin{Bmatrix} \sigma_x \\ \sigma_y \\ \tau_{xy} \end{Bmatrix} dz = \int_{-t/2}^{t/2} [\bar{Q}] \begin{Bmatrix} \varepsilon_x \\ \varepsilon_y \\ \gamma_{xy} \end{Bmatrix} dz = \int_{-t/2}^{t/2} [\bar{Q}] \begin{Bmatrix} \varepsilon_{xo} \\ \varepsilon_{yo} \\ \gamma_{xyo} \end{Bmatrix} dz + \int_{-t/2}^{t/2} [\bar{Q}] \begin{Bmatrix} k_x \\ k_y \\ k_{xy} \end{Bmatrix} z dz \tag{1.15}$$

$$\begin{Bmatrix} M_y \\ M_x \\ M_{xy} \end{Bmatrix} = \int_{-t/2}^{t/2} \begin{Bmatrix} \sigma_x \\ \sigma_y \\ \tau_{xy} \end{Bmatrix} z dz = \int_{-t/2}^{t/2} [\bar{Q}] \begin{Bmatrix} \varepsilon_x \\ \varepsilon_y \\ \gamma_{xy} \end{Bmatrix} z dz =$$

$$= \int_{-t/2}^{t/2} [\bar{Q}] \begin{Bmatrix} \varepsilon_{xo} \\ \varepsilon_{yo} \\ \gamma_{xyo} \end{Bmatrix} z dz + \int_{-t/2}^{t/2} [\bar{Q}] \begin{Bmatrix} k_x \\ k_y \\ k_{xy} \end{Bmatrix} z^2 dz \tag{1.16}$$

With the use of the stiffness matrices of the laminate, equations (1.15),(1.16) can be written in the following form:

$$\begin{Bmatrix} N_x \\ N_y \\ N_{xy} \end{Bmatrix} = [A] \begin{Bmatrix} \varepsilon_{xo} \\ \varepsilon_{yo} \\ \gamma_{xyo} \end{Bmatrix} + [B] \begin{Bmatrix} k_x \\ k_y \\ k_{xy} \end{Bmatrix} \tag{1.17}$$

$$\begin{Bmatrix} M_x \\ M_y \\ M_{xy} \end{Bmatrix} = [B] \begin{Bmatrix} \varepsilon_{xo} \\ \varepsilon_{yo} \\ \gamma_{xyo} \end{Bmatrix} + [D] \begin{Bmatrix} k_x \\ k_y \\ k_{xy} \end{Bmatrix} \tag{1.18}$$

where [A] is the extensional stiffness matrix, [B] is the coupling stiffness matrix and the [D] is the bending stiffness matrix, the elements of which are calculated as following:

$$A_{ij} = \int_{-t/2}^{t/2} [\bar{Q}] dz = \sum_{k=1}^{K} (\bar{Q}_{ij})_k (z_k - z_{k-1}) \tag{1.19}$$

$$B_{ij} = \int_{-t/2}^{t/2} [\bar{Q}] z dz = \frac{1}{2} \sum_{k=1}^{K} (\bar{Q}_{ij})_k ({z_k}^2 - {z_{k-1}}^2) \tag{1.20}$$

$$D_{ij} = \int_{-t/2}^{t/2} [\bar{Q}] z^2 dz = \frac{1}{3} \sum_{k=1}^{K} (\bar{Q}_{ij})_k ({z_k}^3 - {z_{k-1}}^3) \tag{1.21}$$

where K is the total number of the plies in the laminate, z_k, z_{k-1} are the distances from the middle plane to the two surfaces of the ply-k (figure 1.6) and $(\bar{Q}_{ij})_k$ are the elements of the stiffness matrix of the ply-k

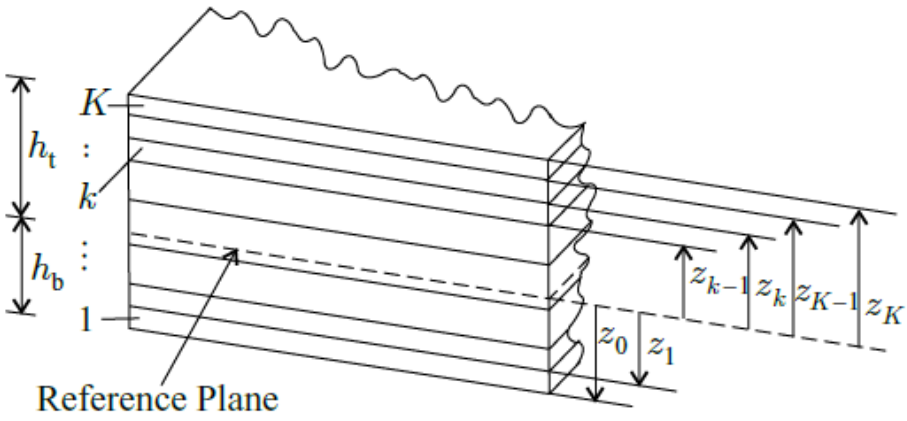

Figure 1.6 : Distance from the reference plane [28]

The extensional stiffness matrix [A] relates the in-plane forces to the in-plane deformations, the bending stiffness matrix [D] relates the moments to the curvatures, while the coupling stiffness matrix [B] relates the in-plane forces to the curvatures and the moments to the in-plane deformations.

Interlaminar stresses

The laminate plate theory is based on the assumption that the laminate, as well as each separate layer are in plane-stress state, thus all the out-of-plane stresses are considered to be zero. This assumption is accurate in regions far from the laminate's free edges, however, it is not accurate near the free edges, where both normal and shear stresses may arise between the layers. These interlaminar stresses can affect the stress field that exists away from the free edges and can have as a result the onset of cracks in the free edges which can lead to separation of the adjacent layers [28].

1.6.3 Sandwich plates

The behavior of thin plates undergoing small deformations can be analyzed based on the Kirchhoff hypothesis, however, this assumption is not accurate in the case of sandwich plates, because normal do not necessarily remain perpendicular to the reference plane. In this case the x and y displacements of a point of the sandwich plate are given by the following equations.

$$u = u_o - z\,\chi_{xz} \qquad v = v_o - z\,\chi_{yz} \tag{1.22}$$

Where u_o , v_o are the x and y displacements at the reference plane, χ_{xz}, χ_{yz} are the notations of the normal in the x-z and y-z planes and z is the distance of the point from the reference plane.

The strains at the reference plane are:

$$\varepsilon_{xo} = \frac{\partial u_o}{\partial x}\,, \qquad \varepsilon_{yo} = \frac{\partial v_o}{\partial y}\,, \quad \gamma_{xyo} = \frac{\partial u_o}{\partial y} + \frac{\partial v_o}{\partial x} \tag{1.23}$$

The transverse shear strains are:

$$\gamma_{xz} = \frac{\partial w_o}{\partial x} - \chi_{xz}\,, \qquad \gamma_{yz} = \frac{\partial w_o}{\partial y} - \chi_{yz} \tag{1.24}$$

Where w_o is the deflection of the reference plane.

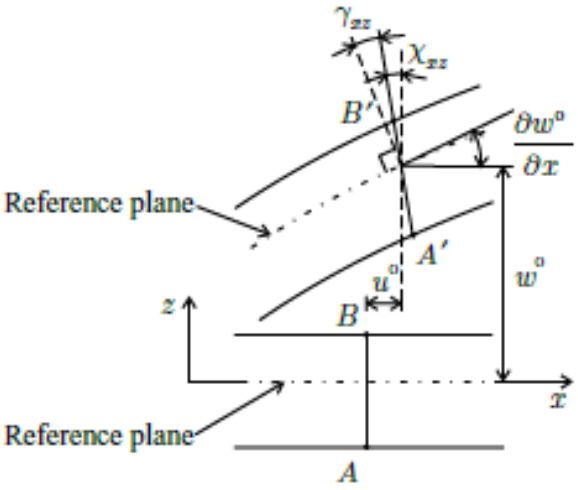

Figure 1.7: Deformation of a sandwich plate in the x-z plane [28]

The resulting strains at a distance z from the reference plane are given by equations (1.25)

$$\varepsilon_x = \frac{\partial u}{\partial x} = \frac{\partial u_o}{\partial x} - z\frac{\partial \chi_{xz}}{\partial x}$$

$$\varepsilon_y = \frac{\partial v}{\partial y} = \frac{\partial v_o}{\partial y} - z\frac{\partial \chi_{yz}}{\partial y} \tag{1.25}$$

$$\gamma_{xy} = \frac{\partial u}{\partial y} + \frac{\partial v}{\partial x} = \frac{\partial u_o}{\partial y} + \frac{\partial v_o}{\partial x} - z\left(\frac{\partial \chi_{xz}}{\partial y} + \frac{\partial \chi_{yz}}{\partial x}\right)$$

Considering a plane-stress condition the stresses can be calculated by equation (1.26)

$$\begin{Bmatrix} \sigma_x \\ \sigma_y \\ \tau_{xy} \end{Bmatrix} = \begin{bmatrix} \bar{Q}_{11} & \bar{Q}_{12} & \bar{Q}_{16} \\ \bar{Q}_{12} & \bar{Q}_{22} & \bar{Q}_{26} \\ \bar{Q}_{16} & \bar{Q}_{26} & \bar{Q}_{66} \end{bmatrix} \begin{Bmatrix} \varepsilon_x \\ \varepsilon_y \\ \gamma_{xy} \end{Bmatrix} \tag{1.26}$$

The in-plane forces, the moments and the transverse shear forces can then be calculated by (1.27), (1.28) and (1.29).

$$\begin{Bmatrix} N_x \\ N_y \\ N_{xy} \end{Bmatrix} = \int_{-h_b}^{h_a} \begin{Bmatrix} \sigma_x \\ \sigma_y \\ \tau_{xy} \end{Bmatrix} dz = [A] \begin{Bmatrix} \varepsilon_{xo} \\ \varepsilon_{yo} \\ \gamma_{xyo} \end{Bmatrix} + [B] \begin{Bmatrix} -\dfrac{\partial \chi_{xz}}{\partial x} \\ -\dfrac{\partial \chi_{yz}}{\partial y} \\ -\dfrac{\partial \chi_{xz}}{\partial y} - \dfrac{\partial \chi_{yz}}{\partial x} \end{Bmatrix} \tag{1.27}$$

$$\begin{Bmatrix} M_y \\ M_x \\ M_{xy} \end{Bmatrix} = \int_{-h_b}^{h_a} \begin{Bmatrix} \sigma_x \\ \sigma_y \\ \tau_{xy} \end{Bmatrix} z dz = [B] \begin{Bmatrix} \varepsilon_{xo} \\ \varepsilon_{yo} \\ \gamma_{xyo} \end{Bmatrix} + [D] \begin{Bmatrix} -\dfrac{\partial \chi_{xz}}{\partial x} \\ -\dfrac{\partial \chi_{yz}}{\partial y} \\ -\dfrac{\partial \chi_{xz}}{\partial y} - \dfrac{\partial \chi_{yz}}{\partial x} \end{Bmatrix} \tag{1.28}$$

$$\begin{Bmatrix} V_x \\ V_y \end{Bmatrix} = \int_{-h_b}^{h_a} \begin{Bmatrix} \tau_{xz} \\ \tau_{yz} \end{Bmatrix} dz = \begin{bmatrix} \bar{S}_{11} & \bar{S}_{12} \\ \bar{S}_{12} & \bar{S}_{22} \end{bmatrix} \begin{Bmatrix} \gamma_{xz} \\ \gamma_{yz} \end{Bmatrix} \tag{1.29}$$

Where $[\bar{S}]$ is the sandwich plate's shear stiffness matrix and h_b, h_a are the distances of the bottom and the top plate, from the reference plane.

2. Introduction to the thesis subject

2.1 Scope of thesis

Subject thesis falls into a general context of research on a problem proposed by Bureau Veritas. Bureau Veritas is a company specialized in testing, inspection and certification, widely known in the marine sector.

The mechanical tests conducted by Bureau Veritas for the verification of the mechanical characteristics of composite materials are described in NR546 rules. One of the tests included in NR546 rules is a test for the characterization of the shear properties of sandwich material panels, based on the standard ISO 14125. This standard refers to a 3 or 4-point bending test which can be easily conducted, but has disadvantages, such as the fact that tested specimens do not always fail due to shear.

Based on the above, Bureau Veritas is considering performing another test, as described by the ASTM C273 standard, which is a test method for the determination of the shear properties of the core in sandwich materials, whose implementation is, however, much more costly.

Tests based on both standards have been conducted and Bureau Veritas is in the process of examining which of the two tests should be preferred.

The shear stiffness of the core is a parameter that significantly affects the failure modes of sandwich structures under in plane loading. Of all the factors that influence the sandwich material's failure initiation modes, the properties of the core material are usually the most predominant [1]. For that reason, having an accurate way of calculating the core's shear characteristics is of great importance.

The scope of the thesis is to model the two tests conducted, with emphasis given on the ISO 14125 standard test, in order to investigate which are the failure mechanisms that occur.

2.2 Description of the two testing standards

2.2.1. ISO 14125 – Three and Four-point bending test

This International Standard specifies a method for determining the flexural properties (flexural strength, flexural modulus and other aspects of the flexural stress/strain relationship) of fiber reinforced plastic composites under three-point (Method A) and four-point (Method B) bending. The tested specimen is deflected at a constant rate until fracture or deformation larger than a pre-determined value are observed. During this procedure, the force applied to the specimen and the specimen's relevant deflection are measured.

Supports and loading member(s) shall be arranged as per figure 2.1. with the distance between them adjustable and their axes parallel to each other. The radii R1 and R2 of the loading member(s) and the supports should be as mentioned in table 2.1, where h is the total thickness of the specimen.

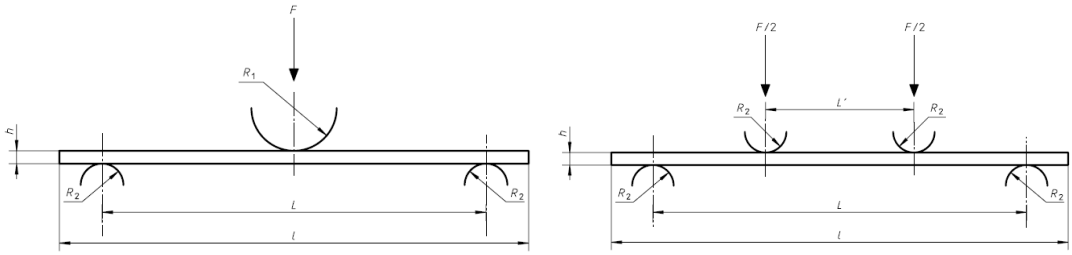

Figure 2.1: 3-point (left) and 4-point (right) bending tests

Table 2.1. Mechanical properties of typical reinforcing fibers

Radius	Value (mm)
R1	5 ± 0.2
R2 (for h<= 3mm)	2 ± 0.2
R2 (for h>3 mm)	5 ± 0.2

Regarding the specimen dimensions, these depend on the tested material and should either be the same as of the preferred test specimens defined in the standard, or when this in not feasible, the length-thickness ratio of the specimens should be the same as in the preferred test specimens.

The possible failure modes than can be observed in composite specimens during this test are listed in the following figure 2.2.

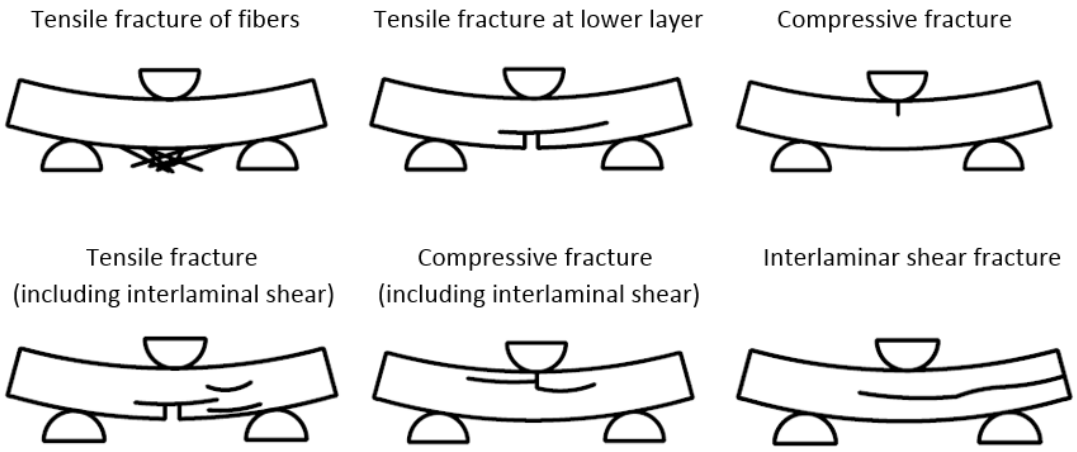

Figure 2.2: Possible failure modes of composites in 3-point bending tests.

In the specific case a sandwich composite is tested based on ISO 14125 or any other three or four-point bending test, the main modes of collapse that are observed are face yield or face microbuckling, wrinkling of the upper face sheet, core shear and indentation, which are shown in figure 2.3. Core shear failure is usually observed in sandwich beams with relatively thick faces and small spans [6].

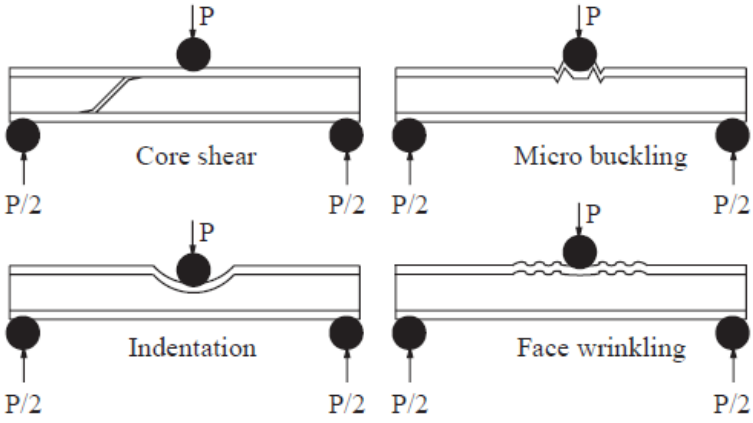

Figure 2.3: Main collapse modes in bending of sandwich composites.

In order to obtain accurate results, a number of at least five specimens have to be tested. For the determination of flexural properties, only tensile-initiated and compression-initiated failures modes, remote from the loading points, are considered acceptable. Whereas for the shear determination, only shear failure modes are acceptable.

Since this standard is specifically created for determining the flexural properties of the tested specimens, no formulas are given for the calculation of the arising shear stresses.

2.2.2. ASTM C273

This test method covers the determination of shear properties of sandwich core materials associated with shear distortion of planes parallel to the facings. It may be conducted on core materials bonded directly to the loading plates or the sandwich skins bonded to the plates. The core or sandwich panel is subjected to monotonically increasing shear force parallel to the plane of its faces, by applying opposite tensile or compressive forces to the bonded plates.

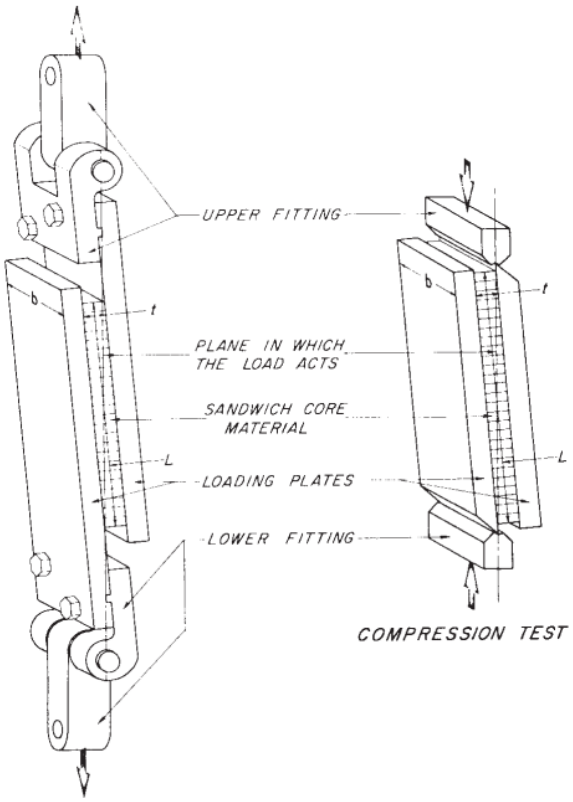

Figure 2.4: ASTM C273 testing standard

The test does not produce pure shear; however, the length of the specimen is prescribed so that secondary stresses have a minimum effect. The tested specimens shall have a thickness equal to the

thickness of the sandwich, a width not less than 50 mm and a length not less than twelve times the thickness.

A minimum of five specimens have to be tested for accurate results, while those specimens that exhibit different failure modes than 100% shear failure of the core, (such as cohesive failures of the core to plate adhesive or adhesion failures to the core or plates) should be rejected. In case the core material exhibits different characteristics in each direction, with respect to shear strength, separate tests have to be contacted in order to obtain the shear stresses in each of the principal directions.

The shear stresses developed during the test and the shear modulus of the core can be calculated by the following formulas:

$$\tau = \frac{P}{L \cdot b} \tag{2.1}$$

where τ is the core shear stress, P the load applied on the specimen, L the length of the specimen and b the width of the specimen and

$$G = \frac{S \cdot t}{L \cdot b} \tag{2.2}$$

where G is the core's shear modulus, $S = \Delta P/\Delta u$ the slope of initial portion of the load deflection curve, u the displacement of the loading plates and t the thickness of the core.

2.3. Experimental results

Tests following the standards mentioned above, were conducted by Bureau Veritas on the same sandwich composite material. The data of the two tests, as well as information on the specimens and the materials were obtained through a report compiled by Ecole Central de Nantes (ECN). Ecole Central de Nantes mainly worked in modeling the linear response of the tested specimens.

The sandwich composite that was tested was composed of two laminate composite skins of E-glass fibers in polyester matrix and a core made from PVC foam. The top skin was composed by nine layers, one CSM layer on top, four layers with 200 g/m^2 of glass fibers and orientations [-45,90,45,0] and four more layers of 300 g/m^2 with orientations of the fibers [-45,90,45,0]. The bottom skin was similar to the top skin, apart from the CSM layer which existed only in the top skin, thus the bottom skin consisted of 8 layers in total, four layers of 200 g/m^2 with orientations [-45,90,45,0] and four layers with 300 g/m^2 of glass fibers and orientations [-45,90,45,0].

Five specimens of the sandwich material were tested for each one of the two testing standards and in addition, a tensile test on the superior skin, as well as a mass percentage of fibers test were conducted based on the ISO 527 and ISO 1172 standards respectively. The dimensions of the tested specimens for the ISO 14125 and the ASTM C273 tests are listed in the table below.

Table 2.2.: Dimensions of the tested specimens

Specimen dimensions	Three-point bending test (ISO 14125)	Shear test (ASTM C273)
Length (mm)	1200 (800 between the two supports)	250
Width (mm)	49.84	50
Thickness (mm)	23.55	22

Regarding the three-point bending test based on the ISO 14125 standard, only one of the five specimens failed in the interlaminar shear failing mode, thus the results from only this specific specimen were considered for the following analysis [7].

For the shear tests based on the ASTM C273 standard, an average imposed force-displacement curve was created based on the results of all five specimens that were tested. The force-displacement curves of the two experiments, as well as photos of the tested specimens, are presented below.

Figure 2.5: Specimens tested based on the ISO 14125 standard

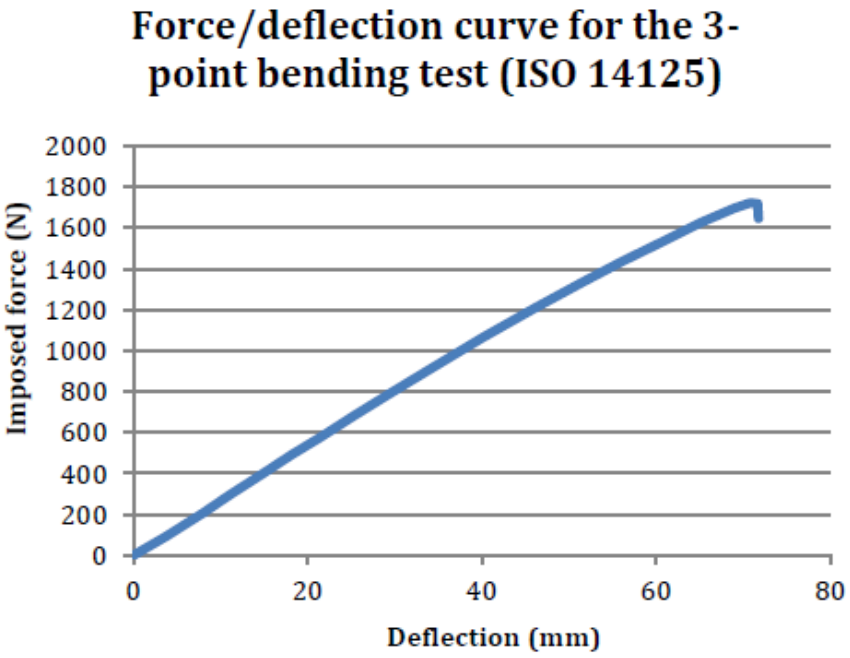

Figure 2.6: Force-deflection curve of the 3-point bending test

Figure 2.7: Specimens tested based on the ASTM C273 standard

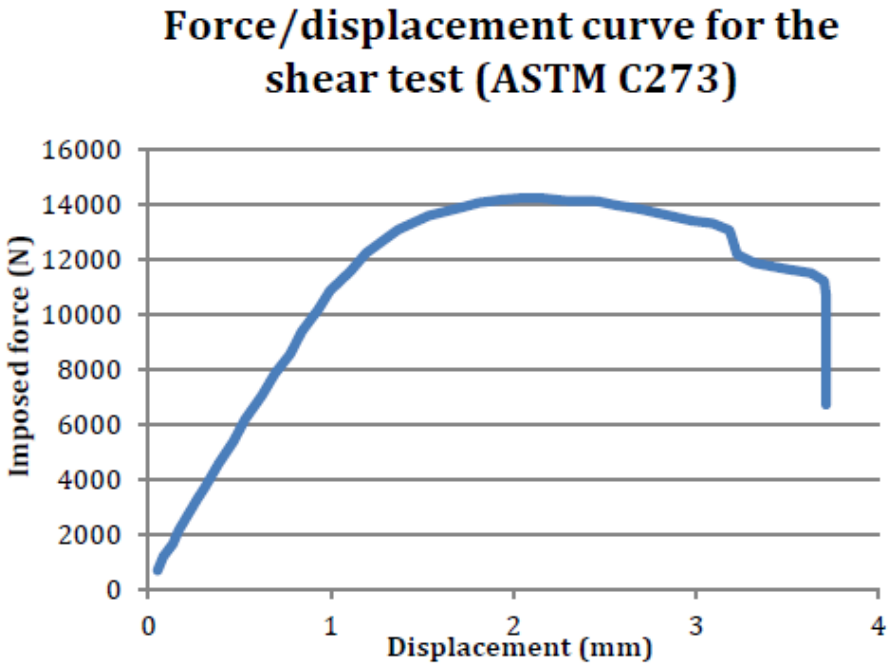

Figure 2.8: Force-displacement curve of the shear test

The results of the conducted tensile test on the superior skin (ISO 527) and of the mass percentage of fibers test (ISO 1172), are gathered in the table below.

Table 2.3.: ISO 1172 and ISO 527 results

Properties	Values
Young Modulus of the superior skin (MPa)	17500
Thickness of the superior skin (mm)	1.65
Mass percentage of fiber (%)	0.70

The shear core moduli calculated by ECN from the 3-point bending and shear test, based on the formulas given in the two standards, had a large deviation from the shear core moduli provided by the supplier. This is shown below in table 2.4.

Table 2.4.: Shear Modulus of core

	Theoretical	3-point bending test	Shear test
Shear Core Modulus (MPa)	27	16	18

Modeling of the specimens' material.

Since not all of the characteristics and mechanical properties of the material of the skins were available (the only available information was the components and orientations of plies, the total mass percentage of fibers of the skins and the Young modulus of the top skin), the skins were modeled by ECN, using the database of Compose, a software developed by Bureau Veritas, which can be used to perform detailed strength analyses of composite panels or stiffeners of ship structures.

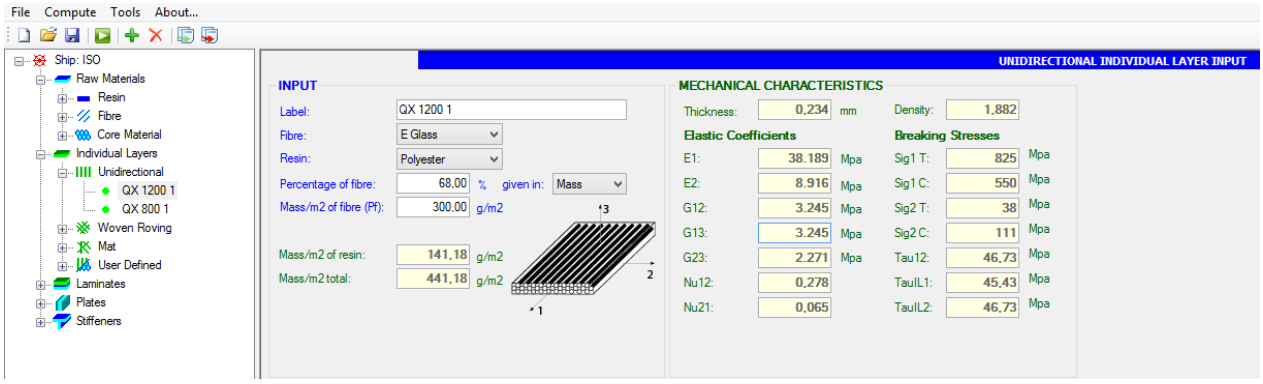

Figure 2.9: ComposeIT software

Based on the modeling by ECN, the constituent layers of the skins and the core of the sandwich composite are considered to have the characteristics shown in table 2.5. The Shear modulus of the core

that was selected does not correspond to the one given by supplier, but to the one obtained through the tests.

Table 2.5.: Modeled material properties

	Foam	QX 1200	QX 800	Mat 300
Thickness (mm)	20	0.234	0.156	0.200
E1 (MPa)	95	38189	38189	23823
E2 (MPa)	95	8916	8916	23823
G12 (MPa)	17	3245	3245	9163
G13 (MPa)	17	3245	3245	2794
G23 (MPa)	17	2271	2271	2794
v12	0.080	0.278	0.278	0.300
v21	0.080	0.065	0.065	0.300
σ1T (MPa)	2.5	825	825	295
σ1C (MPa)	1.4	550	550	295
σ2T (MPa)	2.5	38	38	295
σ2C (MPa)	1.4	111	111	295
τ12 (MPa)	1.15	46.73	46.73	146.60
Mass per m^2 of fibers (g/m^2)	-	300	200	300
Mass percentage of fibers (%)	-	68	68	75
Density (kg/m^3)	80	1.882	1.882	1.999

A schematic of the sandwich material is shown in below figure (2.10).

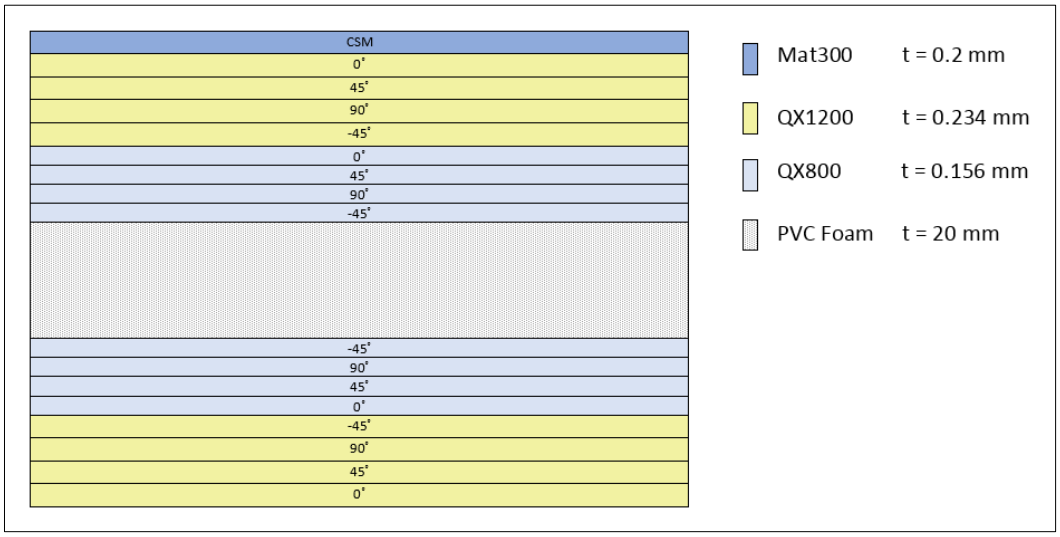

Figure 2.10: Schematic representation of the sandwich specimen

The overall Young Modulus of the superior skin, the thickness of the sandwich and the mass percentage of fibers for the modeled specimen show a very small deviation in comparison to the relevant properties of the tested specimen. A larger deviation is observed in the thickness of the superior skin, however this was considered acceptable, since the Young modulus, rather than the thickness of the skin, is the parameter that mostly affects the response of the specimen [7].

Table 2.6.: Comparison of material modeling and experimental results

	Experimental results	Material modeling
Overall Young Modulus of the top skin (MPa)	17500	17803
Total thickness of the sandwich (mm)	23.55	23.33
Thickness of the top skin (mm)	1.65	1.76
Mass percentage of fiber (%)	0.70	0.69

Shear Stress calculation

ISO 14125 TEST

For a sandwich beam in three-point bending, the predicted collapse load for core failure in shear can be calculated as [6,8]:

$$P = 2\tau_C bd \tag{2.3}$$

where P is the critical force for core shear, b is the sandwich beam width, d is the distance between the centroids of the two skins ($d=c+t_{tf}/2 + t_{bf}/2$,with c being the core thickness and t_{tf}, t_{bf} the thicknesses of the top and bottom skin respectively).

Shear stress can also be calculated using the NF T 54-606 standard, a standard for three-point bending tests of sandwich composites, by the following formula:

$$\tau = \frac{P}{(h + e_\alpha) \cdot b} \tag{2.4}$$

where e_α is the thickness of the core, h the total thickness of the sandwich beam and b is the sandwich beam width.

The Shear stress values calculated using the above equations (2.3), (2.4) are almost identical, showing only a very small deviation. Shear stresses were calculated as an average of these values and are presented below.

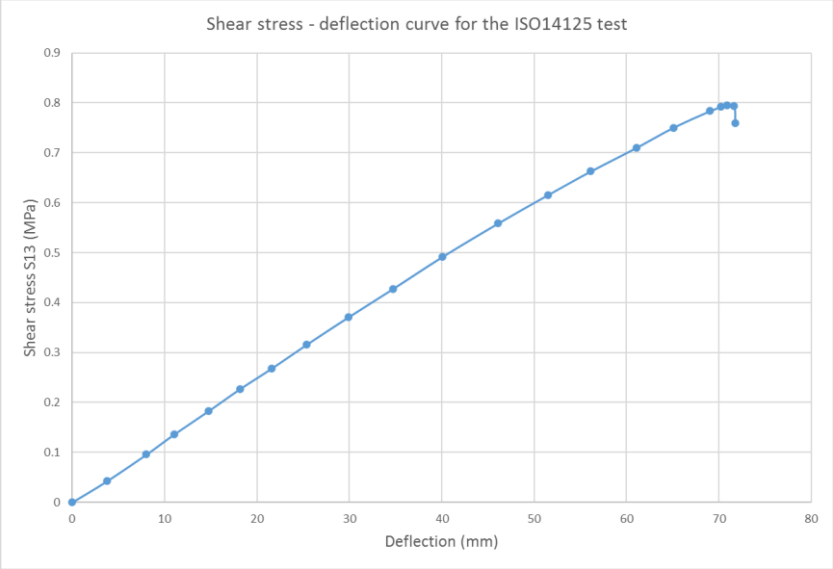

Figure 2.11: Shear stress -deflection curve of the 3-point bending test

ASTM C273 test

Shear stresses for the ASTM C273 test were calculated based on equation (2.1) described in the standard.

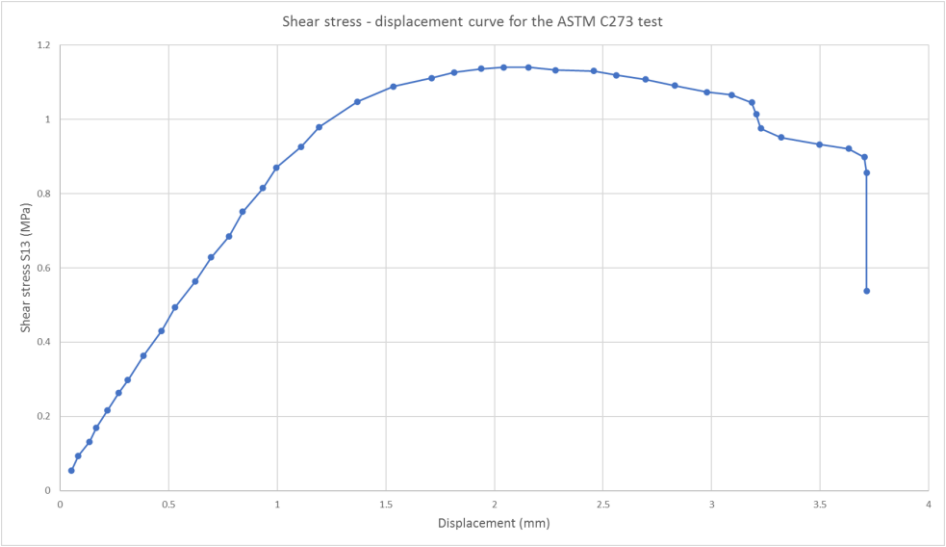

Figure 2.12: Shear stress -displacement curve of the shear test

3. Modeling of the two tests in Abaqus

Abaqus FEM software was used for the modeling of the two tests. The geometry of the problems, the boundary conditions and the loading were defined and tests were simulated.

3.1 Finite Element Analysis

The Finite Element Analysis is a numerical method for solving engineering and mathematical problems. It is very useful in cases where there are complicated geometries, loadings and material properties and thus analytical solutions cannot or are very difficult to be obtained.

To solve the problem, the system is discretized into many smaller parts called finite elements, which are connected to each other on the nodes.

The primary characteristics of a finite element are embodied in the element's stiffness matrix, which contains the geometric and material behavior information that indicates the resistance of the element to deformation. The stiffness matrix [K] corelates the loads applied on the nodes of the elements $\{F\}$ with the relevant displacements $\{U\}$, based on the following equation.

$$\{F\} = [K]\{U\} \tag{3.1}$$

3.1.1. Shape functions

The values of the field variable computed at the nodes are used to approximate the values at non-nodal points with the aid of the shape functions. The shape functions are functions which interpolate the solution between the discrete values obtained at the mesh nodes and are used to describe the variation of the field variable within the finite element. These are usually polynomials derived to satisfy certain conditions at the nodes.

In finite element analysis, solution accuracy is judged in terms of convergence as the element "mesh" is refined. There are two major methods of mesh refinement. In the first, known as h-refinement, mesh refinement refers to the process of increasing the number of elements used to model a given domain, thus reducing the element size. In the second method, p-refinement, element size is unchanged but the order of the polynomials used as interpolation functions is increased.

3.1.2. Solving non-linear problems in Abaqus

Abaqus/Standard uses the Newton-Raphson method to obtain solutions for non-linear problems. In a non-linear analysis the solution usually cannot be calculated by solving a single system of equations, as would be done in a linear problem. Instead, the solution is found by applying the specified loads gradually and incrementally working towards the final solution. Thus, the simulation is broken into a number of load increments and the approximate equilibrium configuration is found at the end of each load increment. It often takes several iterations to determine an acceptable solution to a given load increment. The sum of all the incremental responses is the approximate solution for the nonlinear analysis.

The non-linear response of a structure to a small load increment, ΔP, is shown in figure (3.1). Abaqus/Standard uses the structure's initial stiffness, K_o, which is based on its configuration at u_o, and ΔP to calculate a displacement correction, C_a, for the structure. Using C_a, the structure's configuration is updated to u_a.

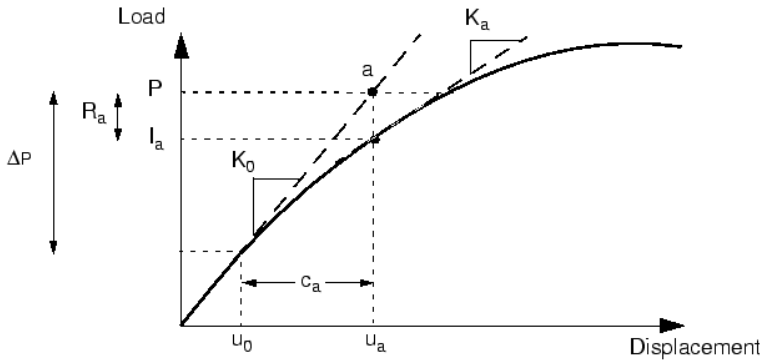

Figure 3.1: First iteration in an increment [40]

Then a new stiffness, Ka, is calculated for the structure, based on its updated configuration, u_a. Abaqus/Standard also calculates I_a, in this updated configuration. The difference between the total applied load, *P*, and I_a are calculated as:

$$R_a = P - I_a \tag{3.2}$$

where R_a is the force residual for the subject iteration.

Abaqus/Standard compares the residual force to a tolerance value and if this is smaller the program accepts the structure's updated configuration as the equilibrium solution.

If the solution from an iteration is not converged, Abaqus/Standard performs another iteration to try to bring the internal and external forces into balance. This second iteration uses the stiffness, Ka, calculated at the end of the previous iteration together with R_a to determine another displacement correction, that brings the system closer to equilibrium.

For each iteration in a non-linear analysis Abaqus/Standard forms the model's stiffness matrix and solves a system of equations. This means that each iteration is equivalent, in computational cost, to conducting a complete linear analysis [40].

3..1.3 Non-linear procedures

If the displacements in a model due to loading are relatively small during a step, the non-linear effects may be small enough to be considered negligible. However, in cases where loads have as a result relatively large displacements of the model, non-linear geometric effects can become important. Non-linear effects can be taken into account in Abaqus by selecting the option Nlgeom, during the loading step.

3.2. Modeling of the ISO 14125 test

Due to the symmetry of the problem, only half of the specimen’s geometry was modeled.

Figure 3.2: Modeled geometry of the 3-point bending test

3.2.1 Part creation

- Loading part - support

The loading part and the support were modeled as three-dimensional analytical rigid parts. Rigid part modeling was chosen as the loading part and the support are much stiffer than the specimen and their deformation can be considered negligible in comparison to the one of the specimen's. Analytical rigid was chosen instead of the discrete rigid part, as this type of part does not need to be meshed, thus this is s computationally less expensive option.

The loading part was created in the form of a quarter of a circle, while the support was created as a circular arc of about 180˚ (analytical rigid shells cannot be created by circular arcs of 180° or more) both with a radius of 5mm, as described in the ISO 14125 standard. The depth of both parts was set to 49.84 mm, same as the width of the tested specimen.

- specimen

The sandwich specimen was modeled as a three-dimensional deformable part with dimensions, 600 mm length, 49.84 mm width and 23.33 mm (as modeled by ECN). The skins were separated from the core by creating partitions on the x-z face of the specimen with the *Partition Face: Sketch option* and then by extruding them along the y-direction using *Partition cell: Extrude sweep edges*.

3.2.2. Property module

Three materials were then created through the material manager, one for the core, one for the UD plies and one for the CSM ply. Material properties were assigned based on the modeling by ECN described earlier.

The material of the core was created with an elastic isotropic behavior, a Young Modulus of 95 MPa and a Poisson ration of 0.08. The materials of the UD and CSM plies were modeled with an elastic mechanical behavior, with the relevant engineering constants defined as per table (2.5).

In this point, materials were assumed to have a linear elastic reponse, thus no failure mechanisms were modeled.

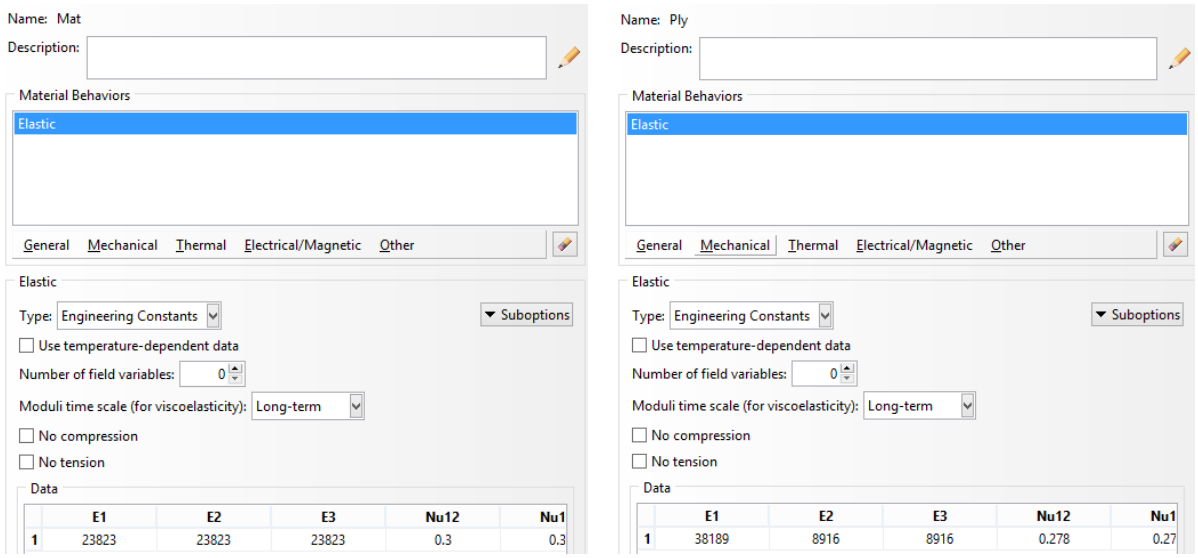

Figure 3.3: Properties of the CSM (left) and UD (right) plies

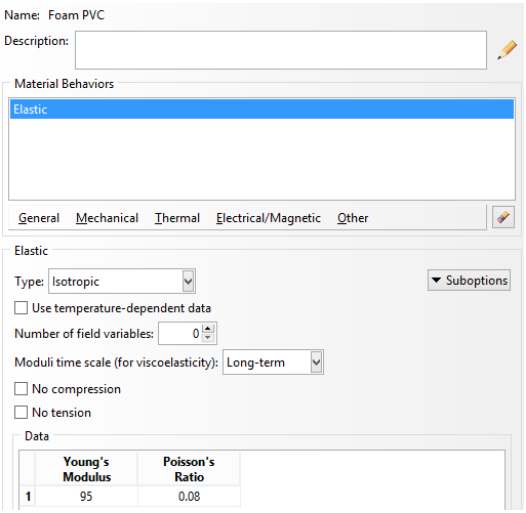

Figure 3.4: Properties of core

A solid homogenous section with the core's material was created for the core and was then assigned on the region of the specimen that corresponds to the core.

Two solid composite layups were then created, one for the top and one for the bottom skin, using the *create composite layup* option and selecting the relevant region of the specimen that corresponds to the subject skin. The composite layup for the top skin was created with 9 plies, whereas the bottom skin with 8 plies, with thickness and fiber orientations as shown in figure 3.4. The plies that are attached to the core are Ply-1 of top skin and Ply-8 of bottom skin.

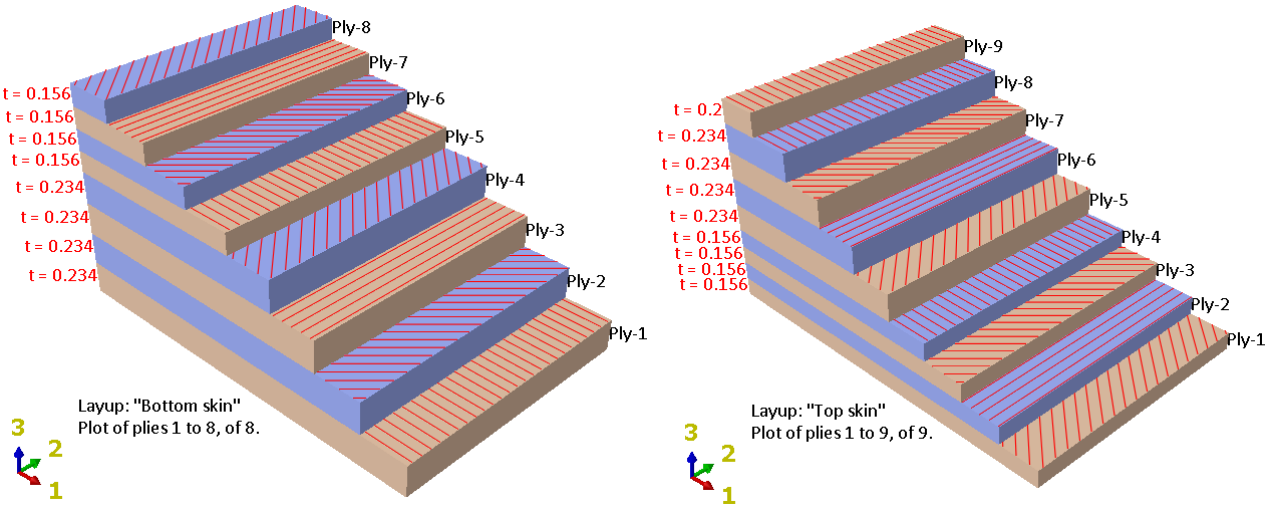

Figure 3.5: Ply stack plot of the bottom and top skin

3.2.3. Assembly module

In the assemby module three instances were created, one for each part, and were then translated and rotated accordingly so that they are positioned as in the three-point bending test. The support was placed at 200 mm distance from the left face of the specimen, while both the support and the loading part where placed 0.5 mm offset from the bottom and top skin respectivelly.

3.2.4. Step module

A static general step was created with automatic incrementation and initial increment size equal to 0.1.

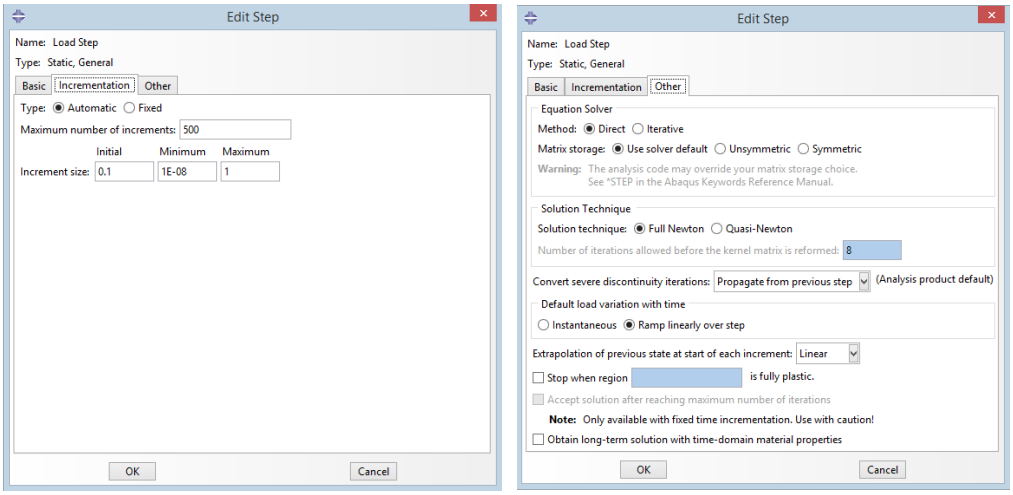

Figure 3.6: Step characteristics

3.2.5. Interaction module

The interactions between the loading part and the specimen and between the support and the specimen were modeled as surface-to-surface contacts during the loading step. The analytical surfaces representing the loading part and the support were selected as the master surfaces, of the two contacts, and the top and bottom surfaces of the specimen were chosen as the slave surfaces. The sliding formulation was selected to be finite sliding, the single confifuration option was selected for the contact tracking and the contact property was defined as of contact type with normal mechanical behavior, characterised by “hard” contact type of pressure-overclosure and default contraint enforcement method.

Rigid body constraints were also created for the loading cylinder and the support by selecting their surfaces ,through the create constraint option for rigid body type, and assigning a reference point to each one of them.

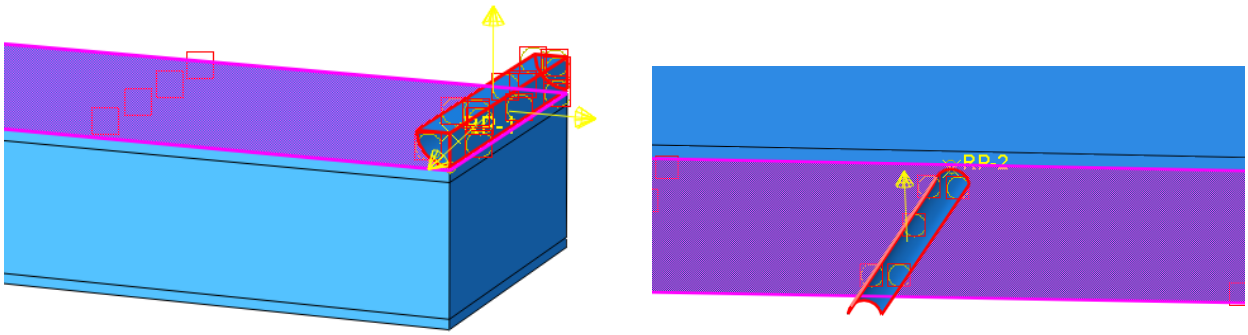

Figure 3.7: Surface-to-surface contact between top skin and loading part and between bottom skin and support

3.2.6. Load module

In the load module, the boundary conditions and the type of loading of the loading part were then defined. For the loading part, displacement control was used instead of load control, by imposing a displacement, rather than a load on this part. All boundary conditions were created in the initial step, apart from the imposed displacement of the loading part, which was created during the load step.

At first, since only half symmetry of the problem was modeled, symmetry along x-direction was defined in the right face of the specimen, by creating a boundary condition, during the initial step, of mechanical category and of symmetry/antisymmetry/encastre type and by then selecting the relevant

surface on the specimen and choosing the XSYMM option. This option restrains the right surface of the specimen from moving along the x-direction and from rotating around the y-axis and z-axis.

The support was encastred by creating a boundary condition of displacement/rotation type, by selecting the reference point of the support and by selecting all the available displacements (U1, U2, U3) and rotations (UR1, UR2, UR3) so that they are all maintained during the loading step.

All displacements and rotations, apart from the displacement along z-direction, where also restricted at the reference point of the loading part, so that it could move only along z-direction.

Lastly, a boundary condition was created for the displacement imposement on the reference point of the loading part, by selecting again the displacement/rotation type and by setting the value of U3 displacement to -70mm (close to the failure deflection of the tested specimen).

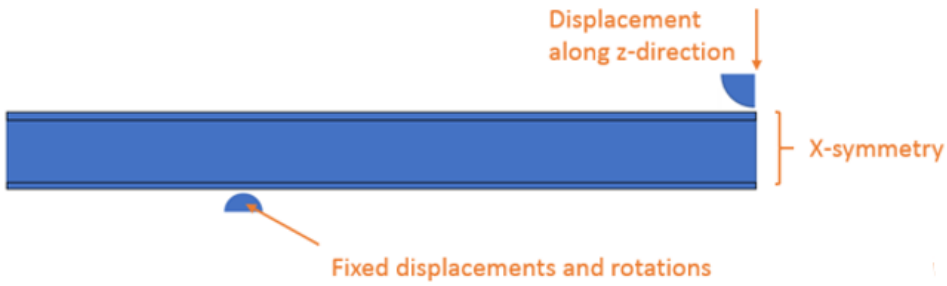

Figure 3.8: Boundary conditions of the problem

3.2.7. Mesh module

Partitions were created on the face of the specimen in order to construct a denser mesh near the region where the loading part comes in contact with the specimen. Hex structured mesh was assigned to the whole specimen through mesh control and three-dimensional linear-hexagonal elements of reduced integration (C3D8R) were selected for all of the specimen's regions.

Meshes of different densities were created, ranging from coarse meshes with 1 element in the thickness of the skin, to fine meshes with 8 elements in the skin thickness.

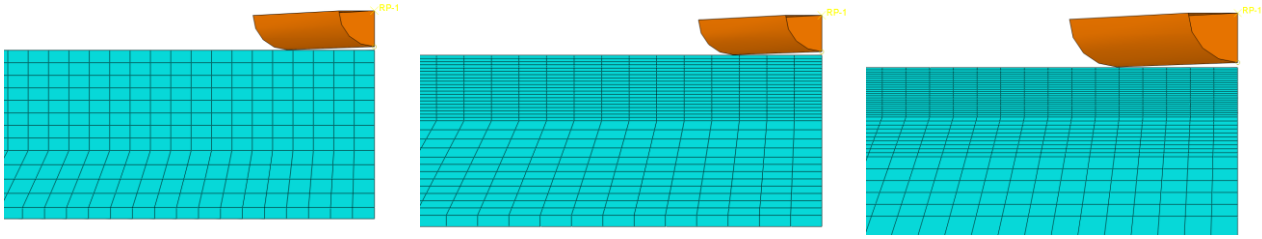

Figure 3.9: Different types of meshes (from left to right): coarse, medium and fine mesh

3.2.8. Simulation results

After performing the simulations for the different mesh-type specimens and by conducting a mesh refinement, the following resulting shear stress-deflection curves were obtained (figure 3.10.)

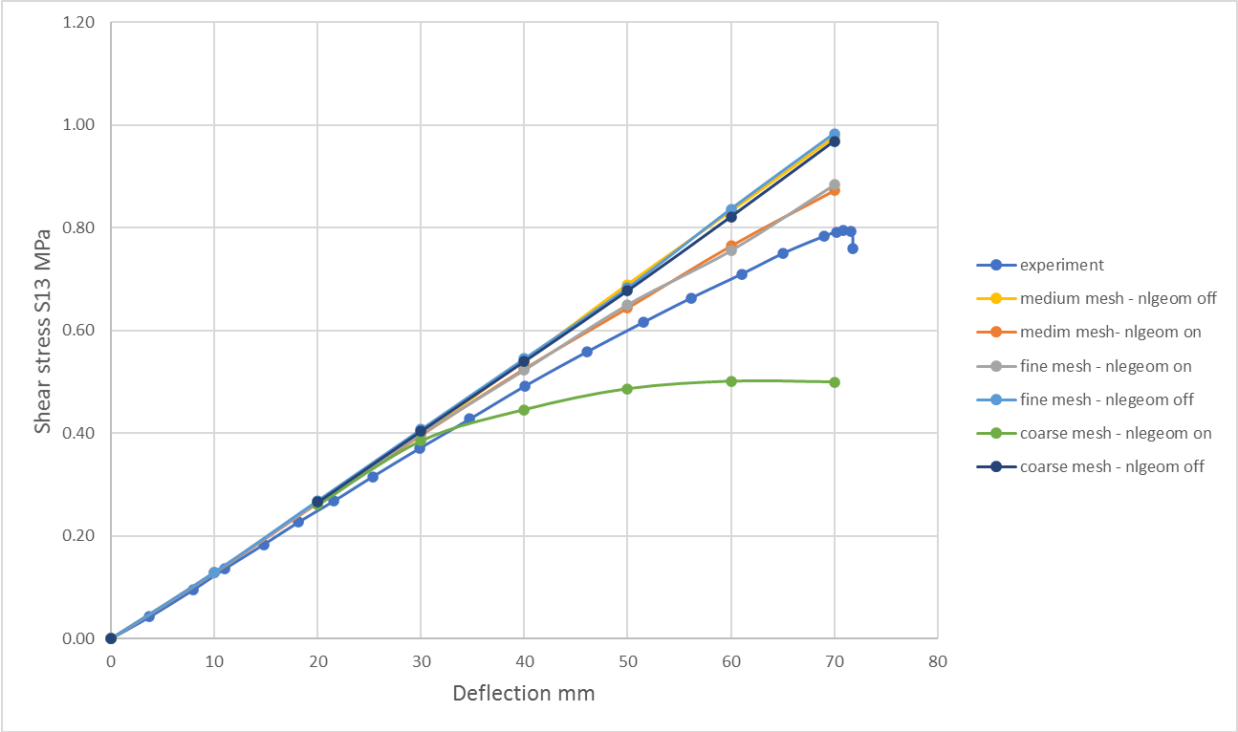

Figure 3.10: Results obtained by the simulations.

As can be seen in figure 3.10. the curves obtained without the non-linear geometry option enabled, are almost identical for the different type of meshes, thus results are not mesh dependent. On the other hand, with the non-linear geometry option enabled, the specimens with medium and fine mesh have

almost the same response, closer to the experimental results, while the specimen with the coarse mesh exbibits lower shear stress values in comparison to the experiment.

3.3. Modeling of the ASTM C273 test

The ASTM C273 can either be applied in sandwich specimens (including both skins and core) or in specimens consisting only of the core. Based on the available photos taken during the experiment, the tested specimens consisted of only the core, thus in order to obtain the most accurate results, same was followed in the modeling of the specimen in Abaqus.

3.3.1. Part creation

Two parts were created for the modeling of the test. The specimen made of core and one of the two loading plates. The specimen was modeled as a three-dimensional deformable solid part with dimensions the same as the ones of the tested specimens (Table 2.2). On the other hand, the loading panel was modeled as a three-dimensional deformable planar shell with its length and width dimensions the same as the ones of the specimen.

3.3.2. Property module

The loading panel was considered to be of steel material with a Young Modulus of E=207 GPa and a Poisson's ratio of v = 0.3. A section of Shell/Continuum shell and Homogenous type with shell thickness 2 mm was created and assigned on the panel.

Regarding the core's material, various models and properties were tested in order to find a proper material that better fits the experimental data. Information regarding the different models tested are given further below. Similarly with above, a section was created for the core material, this time of solid, homogenous type and was assigned on the core.

3.3.3. Assembly and interactions

An instance was created for each one of the parts and these were then assembled accordingly. A tie constraint was used for the bonding of the core's face with the loading panel, with the master surface being the surface of the panel and the slave surface being the surface of the core. In addition, a rigid

body constraint was used on the panel in order to ensure that it would not widstand any deformations during the loading.

3.3.4. Step module

The step created was of type static linear with automatic incrementation and with the Full Newton solution technique.

3.3.5. Load module

The face of the core that was not attached to the panel was constrained using a displacement/rotation type boundary condition by selecting the three displacements U1, U2, U3 to be fixed.

For the loading panel, displacement control was used instead of load control, by imposing a displacement on the reference point of the panel, along the y-direction. All the other degrees of freedom (the two displacements and three rotations) were set to zero.

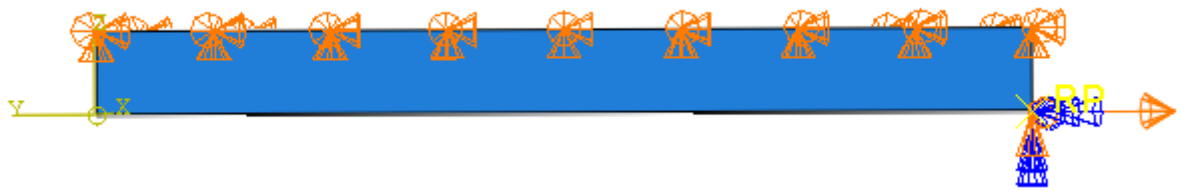

Figure 3.11: Boundary conditions of the problem

3.3.6. Mesh module

Linear shell elements with reduced integration of type S4R where used for the loading panel and three-dimensional linear hexagonal elements with reduced integration, of type C3D8R were chosen for the core.

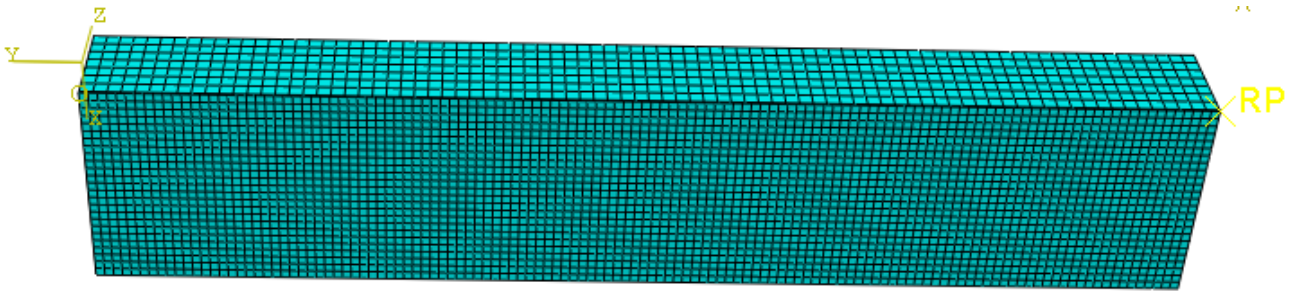

Figure 3.12: Meshing of specimen

3.3.7. Modeling of the core

The core of the sandwich material is made off a cross-linked PVC foam with 80 kg/m3 density. This type of materials are manufactured by melting the bulk polyvinyl chloride (PVC) and by pouring bubbles in the rise direction, process that generates a slight anisotropy in the material [9].

The microstructure of the foam cells in the 1-2 plane has irregular shaped cells, uniformly scatter, giving the foam an isotropic response in this plane. Conversely, in the direction of the thickness, the microstructure of the specimen seems to have more elongated cells. As a result, the foam has a transversely isotropic behavior in the other two planes [10].

Some of the models that have been used in literature for the modeling of PVC foam cores are: the crushable foam modeling with isotropic hardening and the orthrotropic foam modeling with plasticity. Upon research on the values of the elastic properties and strength of the PVC foam core, a variety of models were created in order to investigate which one can better capture the response observed in the test.

The properties that were found in literature, for PVC foams of this density, have been listed in table 3.1.

Table 3.1. Mechanical properties of PVC foams of 80 kg/m3 density.

E tens. (MPa)	E comp. (MPa)	E3 out of plane (Mpa)	G (MPa)	σ0.2% (MPa)	σult comp, (MPa)	σult tens. (MPa)	Shear strength (Mpa)
95.0	90.0		27.0				
76.7				1.16	1.90	1.90	
67.0		116.3	22.8		0.98	2.20	
77.0	77.0	110.0	18.0		1.00	2.30	1.10
66.0	97.0		30.0		1.30	2.00	1.20
77.3			31.0			2.10	1.00
	85.0		31.0				
146.0	85.5		30.0		1.60	2.74	1.20
137.0	68.0		29.0		1.43	2.60	1.13
87.0	92.0		28.0		1.36	1.92	1.37
67.0	75.0		31.0		1.40	2.20	1.10

Based on the above properties and the material modeling techniques proposed in literature, material models with a variety of property values combinations where created in Abaqus and the results obtained from the simulations were then compared to the experimental results. The properties of some

of the models that were created are listed below in table 3.2, with the corresponding simulation results being shown in figure 3.13.

Table 3.2. Characteristics of the core material models created.

Material behaviour		Material Modeling							
		MM_1	MM_2	MM_3	MM_4	MM_5	MM6	MM7	MM8
elastic	type:	isotropic	isotropic	orthotropic	isotropic	orthotropic	orthotropic	isotropic	orthotropic
	E (Mpa)	95	80		95			95	
	v	0.08	0.08		0.08			0.08	
	E1 (Mpa)			77		95	77		95
	E2 (Mpa)			77		95	77		95
	E3 (Mpa)			110		95	110		113
	Nu12			0.08		0.08	0.08		0.08
	Nu13			0.08		0.08	0.08		0.08
	Nu23			0.08		0.08	0.08		0.08
	G12			18		17	18		27
	G13			18		17	18		27
	G23			18		17	18		27
plastic	hardening:			isotropic	isotropic	isotropic	isotropic		isotropic
	yield stress			1.6	2	2	2 / 1.6		1.16/1
	plastic strain			0	0	0	0 / 0.6		0/0.6
crushable foam with hardening	hardening:	isotropic	isotropic					isotropic	
	compression yield stress ratio	1	2					2	
	plastic Poisson's ratio	0.08	0.08					0.08	
	yield stress	2.4	1.6					1.6	
	unizaxial plastic strain	0	0					0	

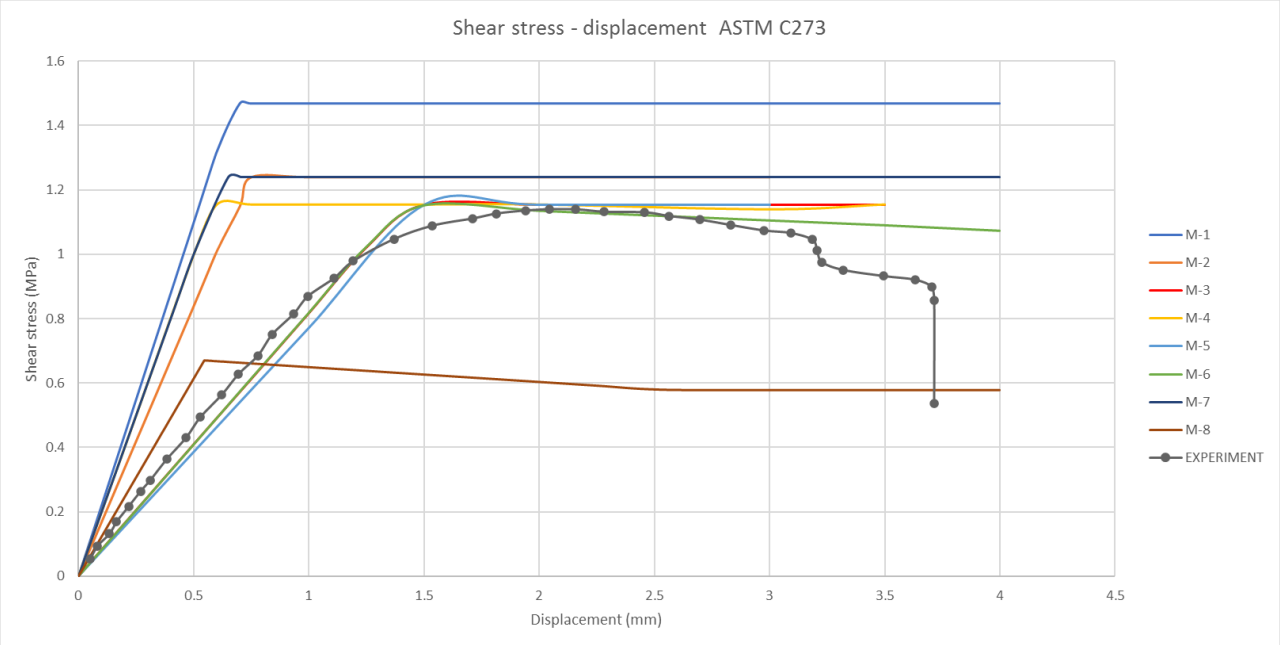

Figure 3.13: Shear stress-displacement curves of the simulation in comparison to the experimental one

From the various materials tried, material model M-6 (Table 3.2) seems to be the one that leads to a better fit to the experimental results.

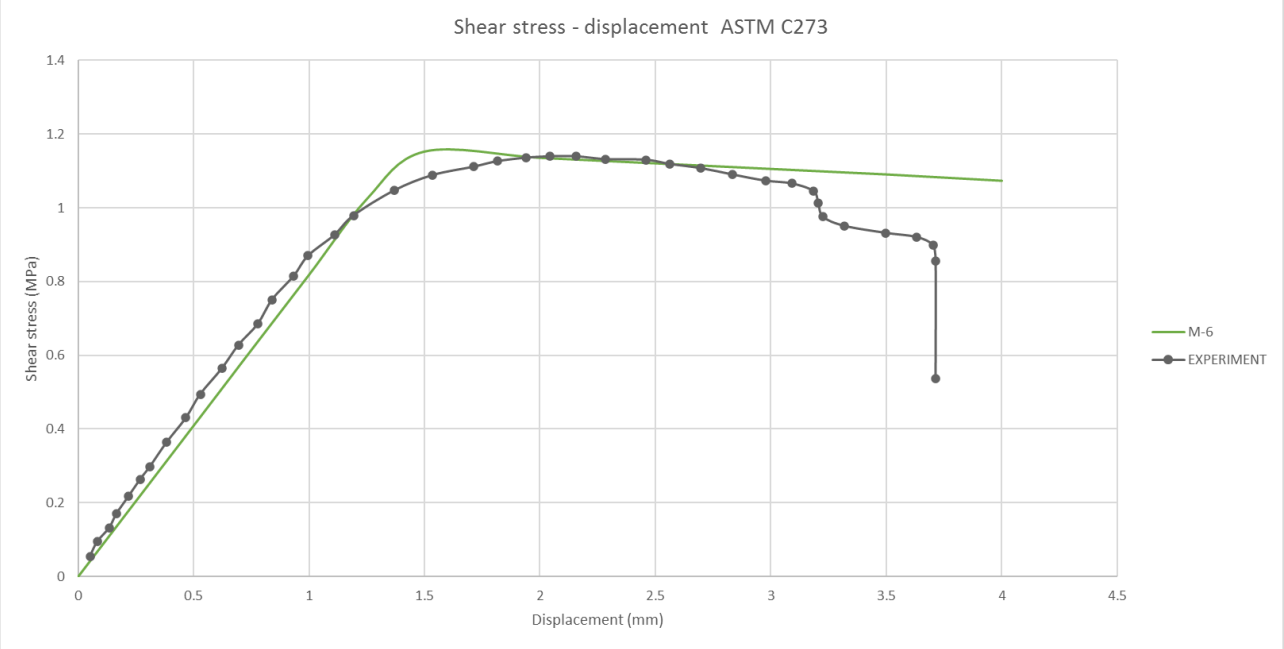

Figure 3.14: Shear stress-displacement curves of the M-6 model and the experiment

4. Modeling of material softening for the 3-point bending test

Upon obtaining results for the elastic linear response of the specimen a next step was the introduction of failure (softening) mechanisms in the materials.

Prediction of failure in composite materials is of great importance while designing composite structures. However, failure in composite materials cannot be easily predicted, as there are various and complex failure modes and mechanisms, which often interact with each other to cause overall failure of the structures. Moreover, the quasi-brittle nature of composite materials means that crack growth can sometimes be extremelly sudden, making it difficult to have an accurate prediction of what amount of damage is necessary for a catastrophic failure to occur [16].

4.1 Skin damage modeling

Failure of sandwich material skins can happen under various modes such as, fiber-matrix debonding, matrix cracking, fiber fracture and delaminations.

Abaqus offers a damage model enabling to predict the initiation of damage and to model damage evolution for fiber-reinforced materials, as are the skins. This damage model requires the specification of the undamaged response of the material, which must be linearly elastic, a damage initiation criterion and a damage evolution response.

4.1.1 Abaqus model for skin damage initiation and propagation

Damage initiation

In Abaqus, damage initiation for fiber reinforced composites is based on Hashin's theory (Hashin and Rotem, 1973, and Hashin, 1980). The damage initiation criteria consider four possible failure modes, namely damage due to fiber tension, fiber compression, matrix tension, and matrix compression.

The damage initiation criteria proposed by Hashin, have they following general forms.

Fiber tension $\hat{\sigma}_{11} \geq 0$

$$F_f^t = \left(\frac{\hat{\sigma}_{11}}{X^T}\right)^2 + \alpha \cdot \left(\frac{\hat{\tau}_{12}}{S^T}\right)^2 \tag{4.1}$$

Fiber compression $\hat{\sigma}_{11} < 0$

$$F_f^c = \left(\frac{\hat{\sigma}_{11}}{X^c}\right)^2 \tag{4.2}$$

Matrix tension $\hat{\sigma}_{22} \geq 0$

$$F_m^t = \left(\frac{\hat{\sigma}_{22}}{Y^T}\right)^2 + \left(\frac{\hat{\tau}_{12}}{S^L}\right)^2 \tag{4.3}$$

Matrix compression $\hat{\sigma}_{22} < 0$

$$F_m^c = \left(\frac{\hat{\sigma}_{22}}{2S^T}\right)^2 + \left[\left(\frac{Y^c}{2S^T}\right)^2 - 1\right] \cdot \frac{\hat{\sigma}_{22}}{Y^c} + \left(\frac{\hat{\tau}_{12}}{S^L}\right)^2 \tag{4.4}$$

where X^T, X^C, Y^T, Y^C, S^T and S^L stand for the longitudinal tensile strength, the longitudinal compressive strength, the transverse tensile strength, the transverse compressive strength, the longitudinal shear strength and the transverse shear strength, respectively.

Coefficient ***a*** is used to determine the contribution of the shear stress to the fiber tensile initiation criterion. Its default value in Abaqus is zero, which corresponds to the model proposed by Hashin and Rotem and can take any other value, including a=1, which corresponds to the model proposed by Hashin.

In addition, $\hat{\sigma}_{11}$, $\hat{\sigma}_{22}$ and $\hat{\tau}_{12}$ refer to the components of the effective shear stress tensor. The effective stress tensor $\hat{\sigma}$ is used to evaluate the damage initiation criteria and is calculated by the following equation.

$$\hat{\sigma} = \mathrm{M} \cdot \sigma \tag{4.5}$$

where M is the damage operator and σ is the real stress tensor

The damage operator M is further calculated by:

$$M = \begin{bmatrix} \frac{1}{1-d_f} & 0 & 0 \\ 0 & \frac{1}{1-d_m} & 0 \\ 0 & 0 & \frac{1}{1-d_s} \end{bmatrix} \tag{4.6}$$

where d_f, d_m and d_s are damage variables for fiber, matrix and shear damage which are derived from the damage variables d_f^t , d_f^c , d_m^t and d_m^c that correspond to the four failure modes.

$$d_f = \begin{cases} d_f^t & if\ \hat{\sigma}_{11} \geq 0 \\ d_f^c & if\ \hat{\sigma}_{11} < 0 \end{cases}$$

$$d_m = \begin{cases} d_m^t & if\ \hat{\sigma}_{22} \geq 0 \\ d_m^c & if\ \hat{\sigma}_{22} < 0 \end{cases} \tag{4.7}$$

$$d_s = 1 - (1 - d_f^t) \cdot (1 - d_f^c) \cdot (1 - d_m^t) \cdot (1 - d_m^c)$$

The values of the four damage initiation criteria F_f^t, F_f^c , F_m^t and F_m^c are represented by the output variables HSNFTCRT, HSNFCCRT, HSNMTCRT and HSNMCCRT respectively. A value less than 1 indicates that the damage initiation criterion has not been satisfied, whereas a value equal to, or higher than 1 indicates that the criterion has been met.

Damage initiation criteria are only used to define whether the material is going to undergo damage under the subject failure modes. However, by defining only the damage initiation properties, the material does not actually undergo any damage. In order for the damage process to be able to be modeled, a relevant damage evolution low has to also be defined. Once an evolution low is defined, then the maximum value that can be obtained by the output variables, representing the damage initiation criteria, is 1. Values higher than 1 are only obtained when the damage evolution law has not been defined and indicate by how much relevant criterion has been exceeded.

The damage initiation criteria for fiber-reinforced materials must be used with elements with a plane stress formulation, which include plane stress, shell, continuum shell, and membrane elements.

Damage evolution

Prior to the damage initiation criterion being fulfilled, the material has a linear elastic response, with a stiffness matrix of a plane stress orthotropic material. Upon the initiation of damage, the material response is calculated by:

$$\sigma = C_d \cdot \varepsilon \tag{4.8}$$

Where ε is the strain and C_d is the damaged elasticity matrix, computed by the following formula.

$$C_d = \frac{1}{D} \cdot \begin{bmatrix} (1-d_f)E_1 & (1-d_f)\cdot(1-d_m)\cdot v_{21}\cdot E_1 & 0 \\ (1-d_f)\cdot(1-d_m)\cdot v_{12}\cdot E_2 & (1-d_m)E_2 & 0 \\ 0 & 0 & (1-d_s)\cdot G\cdot D \end{bmatrix} \tag{4.9}$$

where E_1 is the Young's modulus in the fiber direction, E_2 is the Young's modulus in the matrix direction, G is the shear modulus, v_{12} and v_{21} are the Poisson's ratios and D a parameter calculated by the following equation.

$$D = 1 - \left(1-d_f\right)\cdot(1-d_m)\cdot v_{12}\cdot v_{21} \tag{4.10}$$

In order to reduce the mesh dependency during the softening of the material, Abaqus uses a characteristic length Lc, altering the constitutive law to a stress-displacement relation. The stress-displacement curve has the following form, where the first part with the positive slope corresponds to the linear elastic response prior to damage initiation and the second part with the negative slope corresponds to the evolution of damage.

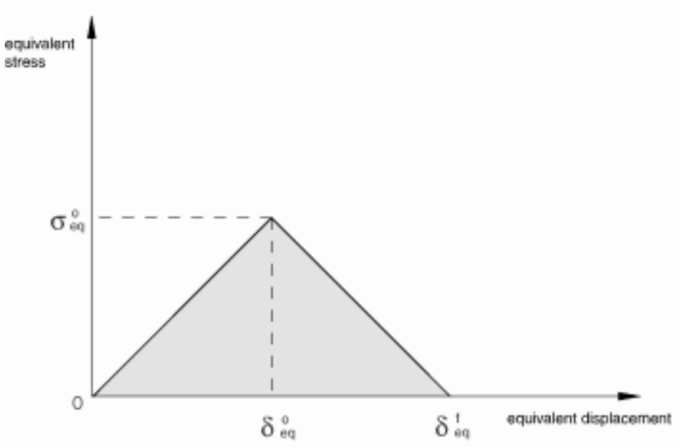

Figure 4.1: Equivalent stress – equivalent displacement curve

The equivalent stress and displacement (figure 4.1) of each failure mode are defined by the following equations.

Fiber tension $\hat{\sigma}_{11} \geq 0$

$$\delta_{eq}^{ft} = L^c\sqrt{\langle\varepsilon_{11}\rangle^2 + \alpha\cdot\varepsilon_{12}^2} \qquad \sigma_{eq}^{ft} = \frac{\langle\sigma_{11}\rangle\cdot\langle\varepsilon_{11}\rangle + \alpha\cdot\tau_{12}\cdot\varepsilon_{12}}{\delta_{eq}^{ft}/L^c} \tag{4.11}$$

Fiber compression $\hat{\sigma}_{11} < 0$

$$\delta_{eq}^{fc} = L^c\cdot\langle-\varepsilon_{11}\rangle \qquad \sigma_{eq}^{fc} = \frac{\langle-\sigma_{11}\rangle\cdot\langle-\varepsilon_{11}\rangle}{\delta_{eq}^{fc}/L^c} \tag{4.12}$$

Matrix tension $\hat{\sigma}_{22} \geq 0$

$$\delta_{eq}^{mt} = L^c\sqrt{\langle\varepsilon_{22}\rangle^2 + \varepsilon_{12}^2} \qquad \sigma_{eq}^{mt} = \frac{\langle\sigma_{22}\rangle\cdot\langle\varepsilon_{22}\rangle + \tau_{12}\cdot\varepsilon_{12}}{\delta_{eq}^{mt}/L^c} \tag{4.13}$$

Matrix compression $\hat{\sigma}_{22} < 0$

$$\delta_{eq}^{mc} = L^c\sqrt{\langle-\varepsilon_{22}\rangle^2 + \varepsilon_{12}^2} \qquad \sigma_{eq}^{mc} = \frac{\langle-\sigma_{22}\rangle\cdot\langle-\varepsilon_{22}\rangle + \tau_{12}\cdot\varepsilon_{12}}{\delta_{eq}^{mc}/L^c} \tag{4.14}$$

The symbol ⟨ ⟩ in above equations represents the Macaulay bracket operator, defined as

$\langle x \rangle = (x+|x|)/2$.

Upon damage is initiated, the damage variable of a particular failure mode is given by the following expression.

$$d = \frac{\delta_{eq}^{f}(\delta_{eq} - \delta_{eq}^{0})}{\delta_{eq}(\delta_{eq}^{f} - \delta_{eq}^{0})} \tag{4.15}$$

where δ_{eq}^{0} is the initial equivalent displacement at which damage initiation occurs and δ_{eq}^{f} is the equivalent displacement at which material is fully damaged under the subject failure mode.

The value of δ_{eq}^{0} for each mode depends on the elastic stiffness and strength parameters specified for the damage initiation, while the value δ_{eq}^{f} depends on the fracture energy G^{C}, which corresponds to the area below the stress-displacement curve.

The damage evolution law for fiber-reinforced materials must be used with elements with a plane stress formulation, which include plane stress, shell, continuum shell, and membrane elements.

4.1.2 Application of the damage model in Abaqus

Alterations to the previous model

As mentioned above, this damage model can only be used with elements with a plane stress formulation, which include plane stress, shell, continuum shell, and membrane elements, thus it cannot be used with the 3D stress elements currently used in the skins. Due to that, the modeling of the specimen was altered by creating three different parts, one for the top skin, one for the bottom skin and one for the core, instead of a single one representing the whole specimen.

The two skins and core where modeled seperatelly as three-dimensional solid parts with dimensions: 600 mm length, 49.84 mm width and thicknesses 1.76 mm for the top skin, 1.56 for the bottom skin and 20 mm for the core.

The previously created solid homogenous section with the core's material was assigned to the part representing the core and two new composite layups were created and assigned to the two skins, similarly with before, with the only difference that they were of continuum shell element type instead of solid type.

Tie constraints were used for the bonding of the two skins with the core, through the *create constraint option.* For the tie constraint between the top skin and core, the bottom surface of the top skin was selected as the master surface and the top surface of the core was selected as the slave surface. Similarly, for the tie constraint between the bottom skin and core, the upper surface of the bottom skin was selected as the master surface and the lower surface of the core was selected as the slave surface.

The only other modification that took place on the model , apart from the modification of the material properties that is analysed in the following paragraph, was the change of the the element type on the mesh. The element type for the core was again chosen as standard/linear/3D stress/hex element with reduced integration (C3D8R), whereas the element type of the two skins was altered to standard/linear/continuum shell/hex element (SC8R). Mesh was again created denser near the region where the specimen comes in contact with the loading part.

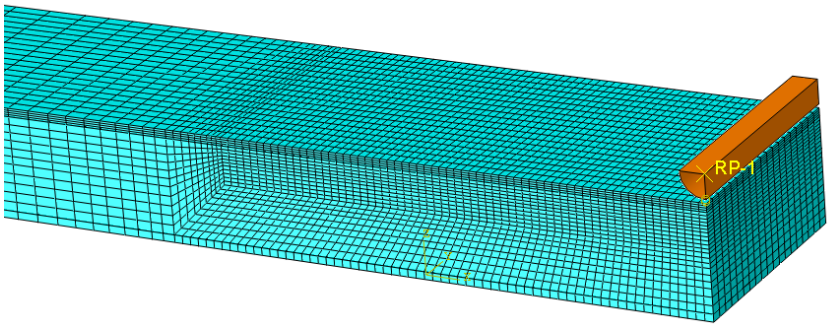

Figure 4.2: Meshing of the specimen

Changes in the material

For the implementation of the Hashin damage initiation criteria and the corresponding damage evolution law, the values of the fracture energies of the four damage modes had to be defined. However, no values could be found in literature for the fracture energies of glass-fibers/polyester matrix composite. The values that were found corresponded to carbon-epoxy plies which, however,

have very large strength in comparison to the plies of the specimen. The only value located for a glass-fibers/polyester ply was the transverse fracture energy. The values that were obtained through literature are gathered in table (4.1). The values marked with * correspond to the UD plies of the tested specimen.

Table 4.1. Ply properties related with skin damage initiation and propagation

Properties	Material		
	carbon-epoxy	carbon-epoxy	glass-polyester
Longitudinal tensile strength (MPa)	2560	2050	825*
Longitudinal compressive strength (MPa)	500	1200	550*
Transverse tensile strength (MPa)	64	62	38*
Transverse compressive strength (MPa)	286	190	111*
Shear strength (MPa)	91.10	81.10	46.73*
Longitudinal tensile fracture energy (kJ/m^2)	81.5	45	-
Longitudinal compressive fracture energy (kJ/m^2)	106.3	45	-
Transerse tensile fracture energy (kJ/m^2)	0.277	0.6	0.9
Transverse compressive fracture energy (kJ/m^2)	0.788	0.6	0.9

Due to the lower strength of the glass fibers, in comparison to the ones made of carbon, the two fractures energies in the fibers direction should be lower for the glass fibers. As an initial assumption the fracture energies of all the fibers where set to 35 kJ/m^2 in the longitudinal direction and to 1 kJ/m^2 in the transverse direction. A sensitivity analysis on these values was conducted by increasing and then decreasing every time one of them to 50% of its value. Results showed that there was no effect on the response by altering these values. Since the CSM layer has lower strength in the longitudinal direction, compared to UD plies its fracture energies in the longitudinal direction were decreased to 15 kJ/m^2. Same values where also given to the fracture energies in the transverse direction, as all the fracture energies should be the same in CSM plies. Another sensitivity analysis on these values was conducted, however, no difference in the results was observed, thus these values where considered acceptable.

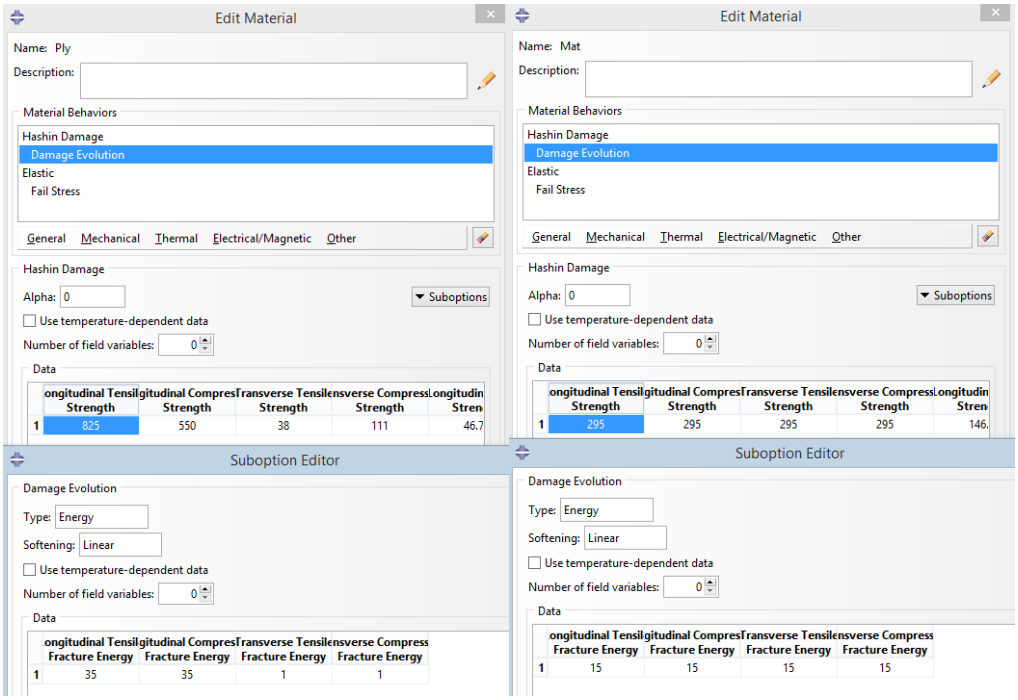

Figure 4.3: Insertion of damage initiation and propagation behavior in the UD and CSM plies

Based on this modeling, the following shear stress – deflection curve was obtained.

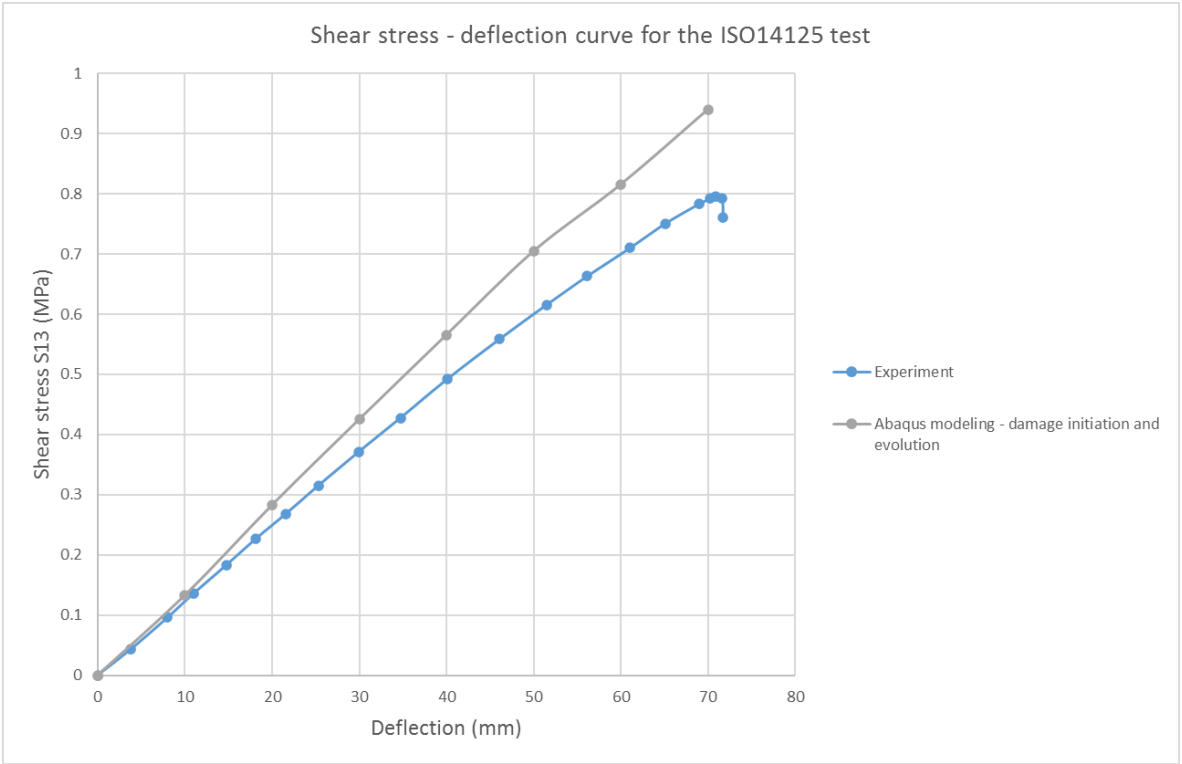

Figure 4.4: Results of skin damage modeling in comparison to the experimental results

4.2 Skin and core damage modeling

The core in the 3-point bending test, was modeled the same as in the shear test. By adding the damage model of the foam in the previous skin damage-model and by running the simulations again, the following results were obtained.

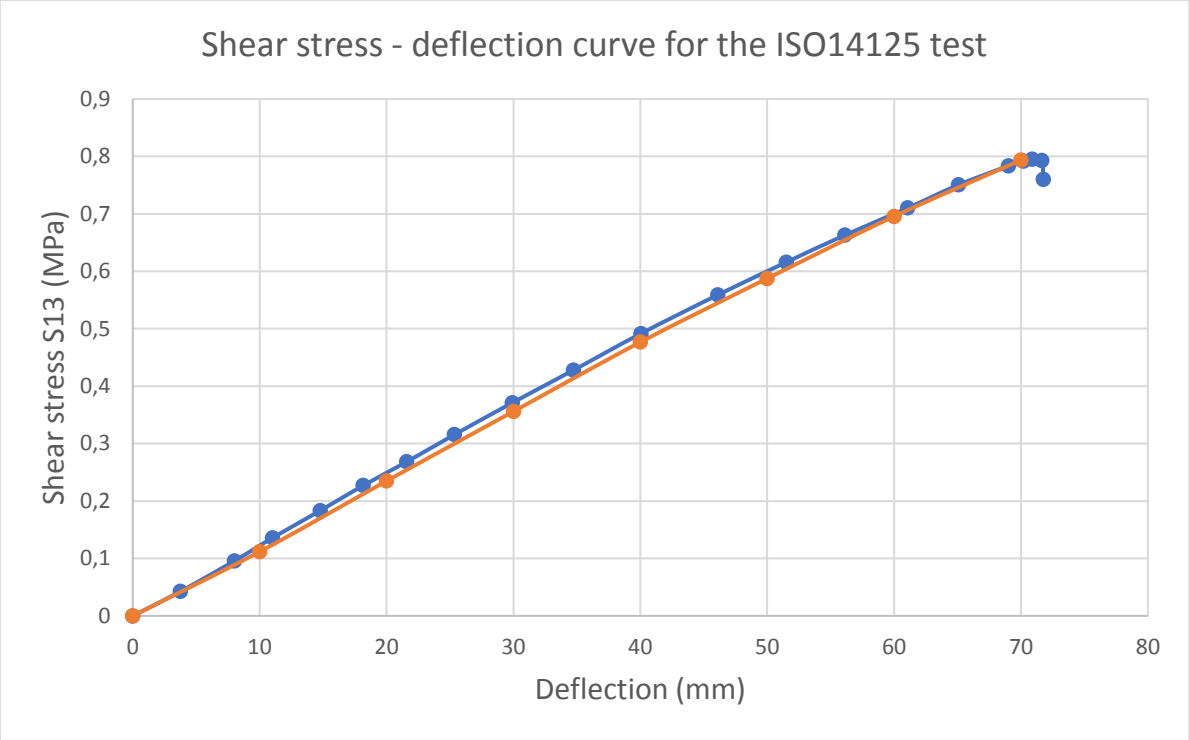

Figure 4.5: Results of skin and core damage modeling in comparison to the experimental results.

Based on the results, damage has been initiaded in almost every single one of the skin plies, apart from plies 1 and 5 of the bottom skin.

In detail, in the top skin plies 1,2,3,5,6 and 7 have been damaged due to matrix failure, with damage initiation sequence 3-7-1-5-2-6 (first ply to be damaged was ply-3 and the last that was damaged was ply-6) and plies 4,8 and 9 have been damaged due to fiber failure with sequence 9-4-8.

In the bottom skin, plies 2,3,4,6,7,8 have been damaged due to matrix failure with sequence 7-3-8-4-2-6.

Since no important plasticity is visible in the core, it is considered that the curve's softening is mainly due to skin damage.

(a) (b) (c)

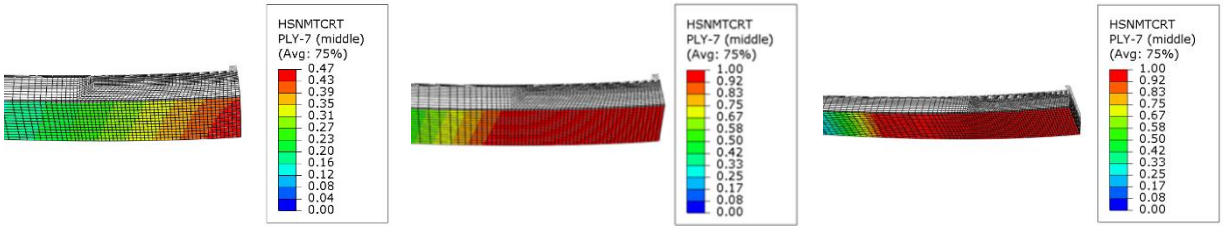

Figure 4.6: Damage evolution of ply-7 of bottom skin at (a) 20 mm (b) 40 mm and (c) 70 mm displacement

(a) (b) (c)

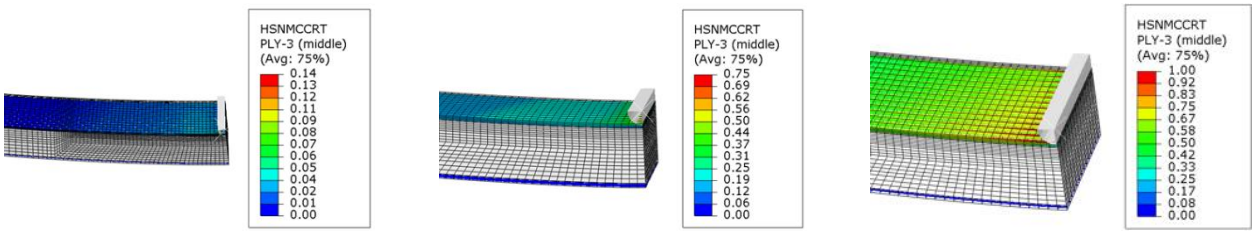

Figure 4.7: Damage evolution of ply-3 of top skin at (a) 20 mm (b) 40 mm and (c) 70 mm displacement

(a) (b) (c)

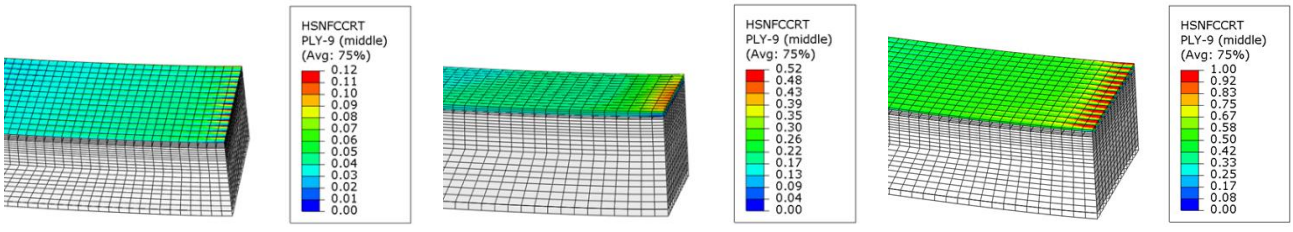

Figure 4.8: Damage evolution of ply-9 of top skin at (a) 20 mm (b) 40 mm and (c) 70 mm displacement

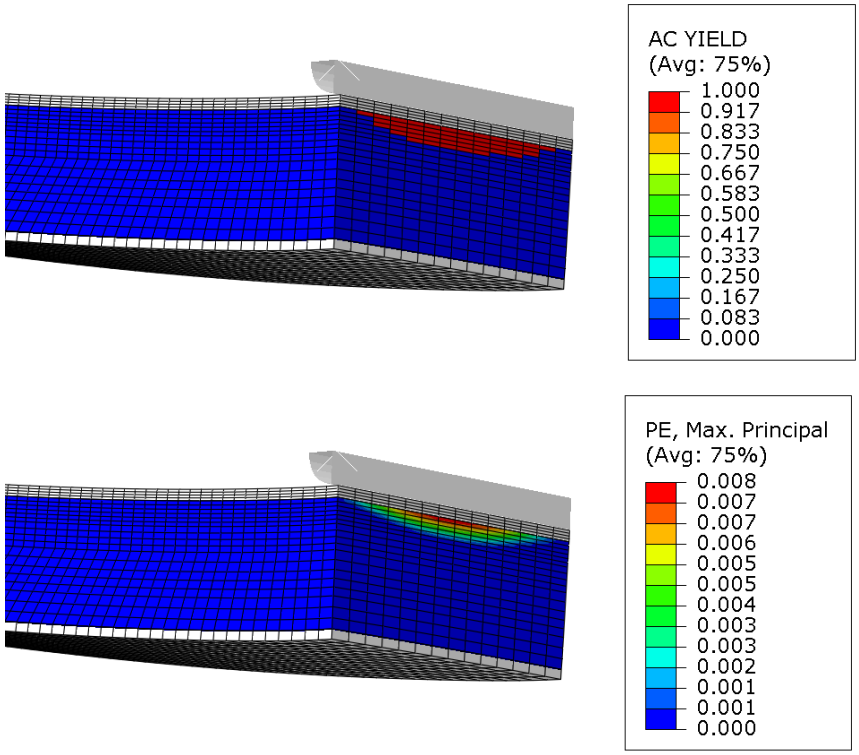

Figure 4.9: Core plasticity at 70mm

By applying larger displacements on the specimen it was noticed that the specimen loses its capacity to carry more load after a displacement of about 107 mm.

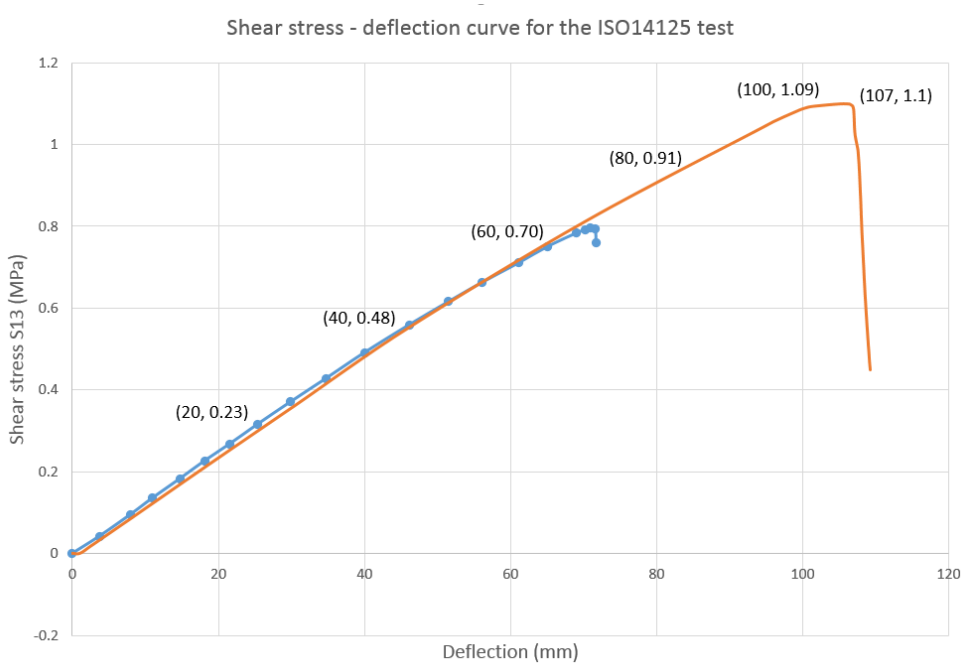

Figure 4.10: Difference in the maximum deflection where failure occurs between modeling and experiment

In below figures can be seen the region of the core where stresses have exceeded the yield stress limit.

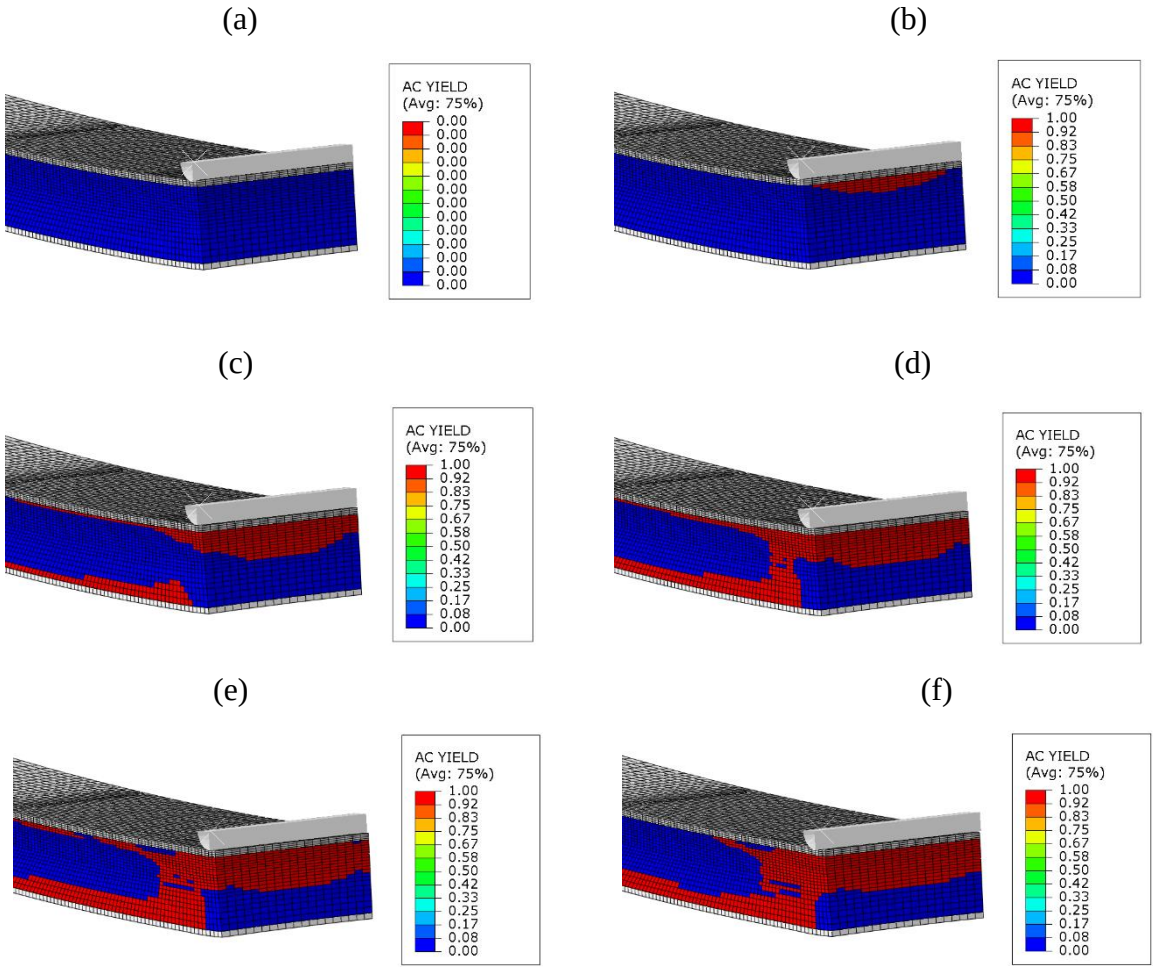

Figure 4.11: Core's plasticity at a displacement of (a) 40mm (b) 60mm, (c) 80mm, (d) 100mm , (e) 104mm and (f) 107mm

In these results non-linear geometric effects were not taken into account since solutions could not converge with the option nlgeomon enabled.

5. Modeling of the core-skin interface debonding

Debonding between the core and the skins of sandwich structures is one of the most critical failure modes of composite materials, as it can lead to loss of the structure's capacity to carry the load [10].

Cracks can be present in the interface of sandwich materials since the stage of production or be created while the sandwich is under loading. Three modes of cracking are usually considered, the opening mode (Mode I), the sliding shear or else called in-plane shearing mode (Mode II) and the tearing shear or out of plane shearing mode (Mode III). The crack tip deformations for the three mentioned modes are presented schematically in figure 5.1.In homogenous materials, crack advance usually happens in mode I, while when a crack advances in the interface of two dissimilar materials, it mostly happens in a mixed mode condition (a combination of the opening modes) [12].

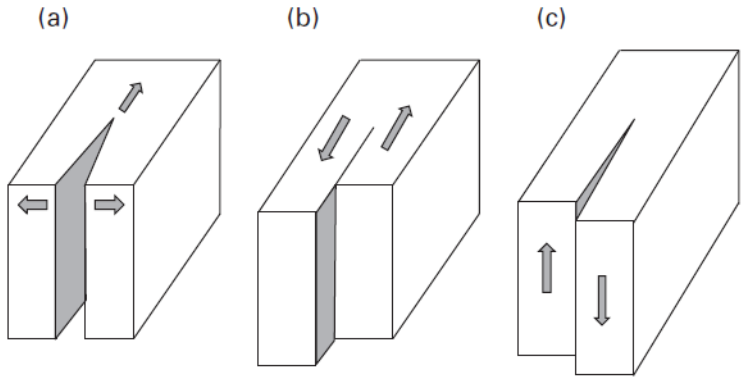

Figure 5.1: Cracking modes: (a) Mode I, (b) Mode II and (c) Mode III

A crack in the skin-core interface of a sandwich structure can propagate in three basic ways. It can propagate within the skin-core interface, it can kink into the core or it can kind into the skin. In case the interface is sufficiently weak and brittle in comparison to the core and the adjacent skin, the crack will most probably propagate in its own plane, through the interface, regardless of the mode mixicity. Conversely, if the interface is tough enough the crack may kink into the skin or core [14]. In sandwich panels with a core of foam material, it has been observed that the skin-core debonding usually propagates inside the core, due to the low fracture resistance of its material [15].

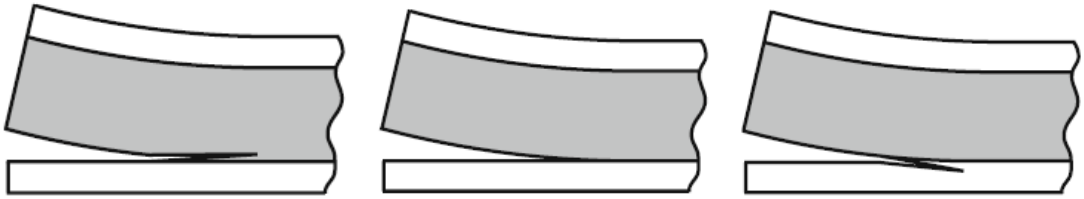

Figure 5.2: Crack propagation paths in the skin-core interface

5.1. Introduction of a pre-crack in the core-skin interface

As a first step, in order to check what is the specimen's response when there is low-scale debonding in the skin-core interface, a pre-crack was inserted in the interface. Crack was introduced in the interface between the top skin and the core, in the region below the loading part, by adjusting the tie constraint between the top skin and core, so that bonding in a small area of the interface was lost.

To ensure that no penetration of the top skin into the core took place, surface to surface contact was introduced between the two faces of the crack. Specimens with a variety of crack lengths were tested, ranging from 5 to 20 mm.

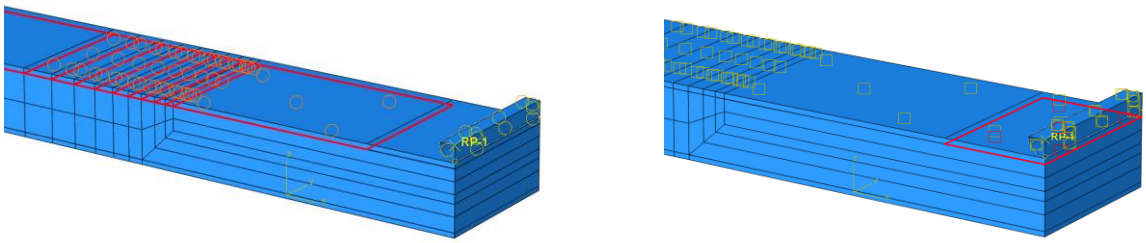

Figure 5.3: Tie constraint between top skin and core (left) and contact between the crack faces (right)

Only minor differences were observed in the values of shear stress in mid-thickness of the specimen for the different crack lengths. With the nlgeom option disabled, the specimen was able to withstand larger deflection in comparison to the experiment, while with the nlgeom option enabled, the specimen failed at lower values of imposed displacement.

In the case where the non-linear geometry was taken into account, it was observed that for all crack lengths tested, all plies of the two skins were damaged and core yield was extended in almost all of the core's thickness. In addition, the specimen lost its capacity to carry further load at lower values of the imposed displacement.

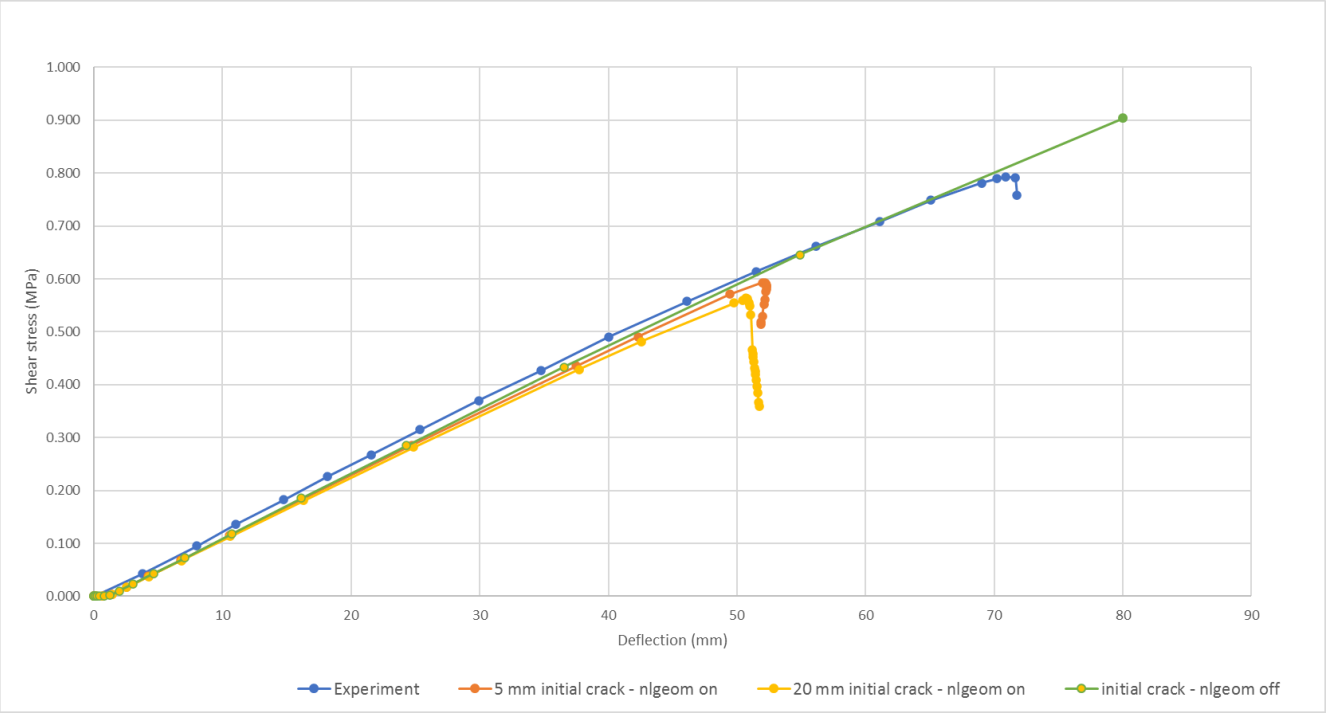

Figure 5.4: Shear stress – deflection curves

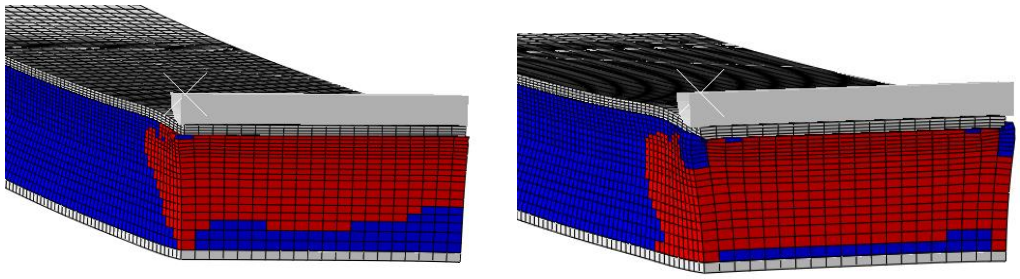

Figure 5.5: Core yield at maximum deflection – nlgeom: specimen with 5 mm crack (left) and with 20 mm crack (right)

5.2. Modeling of the core-skin-interface with cohesive elements

5.2.1 The cohesive zone modelling concept

Cohesive zone-based models have been used in the last years for simulating interface crack propagation in a variety of structures. The concept of cohesive zone modeling is based on modeling separation of two initially bonded surfaces, with the assumption of a softening zone existing ahead of sharp tip in the material. Within this softening zone, the crack opening is resisted by cohesive tractions [16].

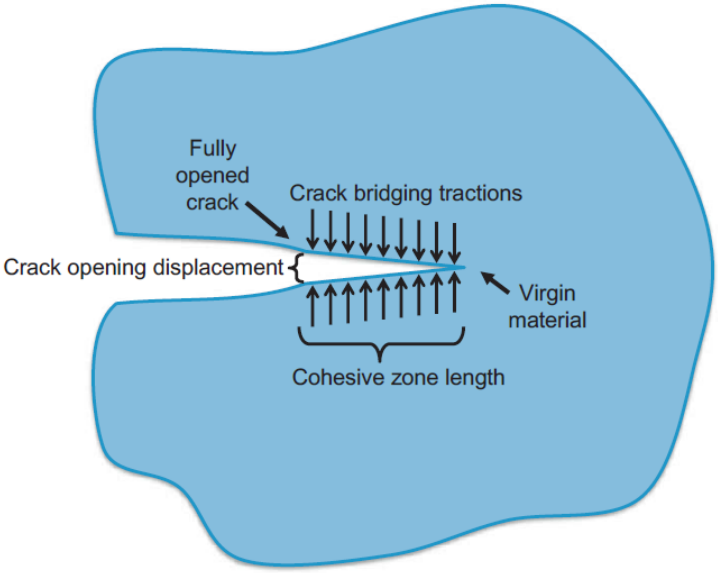

Figure 5.6: Crack opening and cohesive tractions [16]

In cohesive zone modeling, the definition of an initial crack is usually not required, as the initiation and propagation of damage can both be simulated. However, the potential crack path or paths need to be defined a priori [16], fact that poses a problem when the exact path the crack will follow, cannot be predicted. In case the region where the crack is expected to propagate is known, cohesive elements can be inserted between all bulk elements of that region. This, however, may lead to an artificial softening being introduced in the model, altering the material properties and the model's response. Additionally, the solution can usually not converge, thus additional numerical measures need to be taken [17].

5.2.2. Cohesive Zone Modelling in Abaqus

Traction separation response

The traction-separation response of cohesive elements in Abaqus, assumes an initial linear elastic behavior of the elements, which is followed by the initiation and evolution of damage. The elastic response is expressed by an elastic constitutive matrix (stiffness matrix) that relates the nominal stresses to the nominal strains.

$$t = \begin{Bmatrix} t_n \\ t_s \\ t_t \end{Bmatrix} = \begin{bmatrix} K_{nn} & K_{ns} & K_{nt} \\ K_{ns} & K_{ss} & K_{st} \\ K_{nt} & K_{st} & K_{tt} \end{bmatrix} \cdot \begin{Bmatrix} \varepsilon_n \\ \varepsilon_s \\ \varepsilon_t \end{Bmatrix} \tag{5.1}$$

The nominal traction stress vector t, consists of three components in three dimensional problems, t_n which represents the normal traction stress (along the elements local 3-direction – Mode I) and t_t, t_s which represent the two shear tractions (Modes II and III).

The nominal strains are calculated by the corresponding separations δ_n, δs and δt by dividing them with the original thickness of the cohesive element To.

$$\varepsilon_n = \frac{\delta_n}{T_o} \quad , \quad \varepsilon_s = \frac{\delta_s}{T_o} \quad , \varepsilon_t = \frac{\delta_t}{T_o} \tag{5.2}$$

The traction separation law can be either coupled or uncoupled. When coupled, all terms of the elastic matrix [K] must be defined, whereas when the uncoupled option is selected, the values of the off-diagonal terms of the matrix are set to zero. The diagonal terms needed for the uncoupled response can be more easily determined in comparison to the off-diagonal terms and based on studies, the uncoupled model can achieve adequate accuracy. Due to that the uncoupled response is usually preferred in a variety of cases and the coupled response is generally used when the focus is mainly on the cohesive zone [18].

An approximation of the values of the diagonal terms K_{nn}, K_{ss} and K_{tt} can be given by the following formulas. [18,19].

$$Knn = \frac{E_3}{T_o}$$

$$Kss = \frac{2G_{13}}{T_g} \tag{5.3}$$

$$Ktt = \frac{2G_{23}}{T_g}$$

where To is the thickness of the cohesive layers and E_3, G_{13} and G_{23} the elastic moduli of the cohesive layer material.

Damage initiation

The damage or else the degradation of the material of the cohesive elements is initiated when the stresses and/or strains of an element satisfy the damage initiation criterion that have been defined. The damage initiation criteria that are available in Abaqus are these of maximum principal stress, maximum principal strain, maximum nominal stress, maximum nominal strain, quadratic nominal stress and quadratic nominal strain.

maximum principal stress

$$\left\{\frac{\sigma_{max}}{\sigma^o_{max}}\right\} = 1 \tag{5.4}$$

maximum principal strain

$$\left\{\frac{\varepsilon_{max}}{\varepsilon^o_{max}}\right\} = 1 \tag{5.5}$$

maximum nominal stress criterion

$$max\left\{\frac{\langle t_n\rangle}{t_n^o}, \frac{t_s}{t_s^o}, \frac{t_t}{t_t^o}\right\} = 1 \tag{5.6}$$

maximum nominal strain

$$max\left\{\frac{\langle \varepsilon_n\rangle}{\varepsilon_n^o}, \frac{\varepsilon_s}{\varepsilon_s^o}, \frac{\varepsilon_t}{\varepsilon_t^o}\right\} = 1 \tag{5.7}$$

quadratic nominal stress

$$\left\{\frac{\langle t_n \rangle}{t_n^o}\right\}^2 + \left\{\frac{t_s}{t_s^o}\right\}^2 + \left\{\frac{t_t}{t_t^o}\right\}^2 = 1 \tag{5.8}$$

quadratic nominal strain

$$\left\{\frac{\langle \varepsilon_n \rangle}{\varepsilon_n^o}\right\}^2 + \left\{\frac{\varepsilon_s}{\varepsilon_s^o}\right\}^2 + \left\{\frac{\varepsilon_t}{\varepsilon_t^o}\right\}^2 = 1 \tag{5.9}$$

Damage evolution

Damage initiation criteria are only used to define whether the material is going to undergo damage, thus by defining only a damage initiation criterion, the material does not actually undergo any damage. In order to model how the material stiffness is degraded once the damage initiation criterion has been met, a relevant damage evolution low must also be defined.

Once damage has been initiated, the material does no longer have a linear elastic response, with stresses being calculated by equation (5.1). Instead stress components are calculated by following formulas.

$$t_n = \begin{cases} (1-D)\cdot \bar{t}_n \ , \bar{t}_n \geq 0 \\ \bar{t}_n \ , \ \bar{t}_n < 0 \end{cases}$$

$$t_s = (1-D)\cdot \bar{t}_s \tag{5.10}$$

$$t_t = (1-D)\cdot \bar{t}_t$$

Where $\bar{t}_n$, $\bar{t}_s$ and $\bar{t}_t$ are the stress components calculated for the elastic traction-separation response, based on equation (5.1) for the current strains.

There are two parts concerning the evolution of damage. The first part involves specifying either the effective displacement at complete failure, relative to the effective displacement at the initiation of damage, or the energy dissipated due to failure. The second part has to do with specifying the nature of evolution of the damage variable D. Regarding the first part, the option specifying the energy dissipated due to failure, is further analyzed below.

The energy dissipated due to the damage process, or else called the fracture energy, is equal to the area under the traction separation curve. Fracture energy is specified as a material property and can be used in conjunction with a linear or exponential evolution of damage. The dependence of the fracture energy on the mode mix can be specified either directly in a tabular form or by using the following analytical forms.

Power law form

$$\left\{\frac{G_n}{G_n^C}\right\}^{\alpha} + \left\{\frac{G_s}{G_s^C}\right\}^{\alpha} + \left\{\frac{G_t}{G_t^C}\right\}^{\alpha} = 1 \tag{5.11}$$

where $G^C = G_n + G_s + G_t$ is the mixed-mode fracture energy when failure occurs and Gn, Gs and Gt the dissipated energies due to damage in the normal, the first, and the second shear directions, respectively. The parameters that have to be specified for this form are the critical fracture energies of each mode G_n^C, G_s^C and G_t^C, as well as the value of ***a***.

Parameter ***a*** is an empirical parameter derived from a best fit to data from mixed mode bending tests and is generally in the range of 1-2. Some values that have been proposed are a=1 (Hallet -Wisnom), a=1.21 (Pinho) and a=1.23 (Borg) [16].

Benzeggagh-Kenane (BK) form

$$G_n^C + (G_s^C - G_n^C) \cdot \left\{\frac{G_S}{G_T}\right\}^{\eta} = G^C \tag{5.12}$$

where $G_S = Gs + Gt$, $G_T = Gn + Gs$ and η is a material parameter. The parameters that have to be specified for this form are the critical fracture energies G_n^C and G_s^C and the value of η.

With regard to the form of the damage evolution, this can either be linear or exponential, with the damage variable D being defined as per below.

Linear damage evolution

$$D = \frac{\delta_m^f(\delta_m^{max} - \delta_m^o)}{\delta_m^{max}(\delta_m^f - \delta_m^o)} \tag{5.13}$$

where $\delta_m^f = 2G^C/T_{eff}^o$ with T_{eff}^o being the effective traction at damage initiation and δ_m^{max} denotes the maximum value of the effective displacement observed during the loading history.

Exponential damage evolution

$$D = \int_{\delta_m^o}^{\delta_m^f} \frac{T_{eff} \cdot d\delta}{G^C - G_o} \tag{5.14}$$

where Teff is the effective traction, δ the effective displacement and Go the elastic energy at damage initiation.

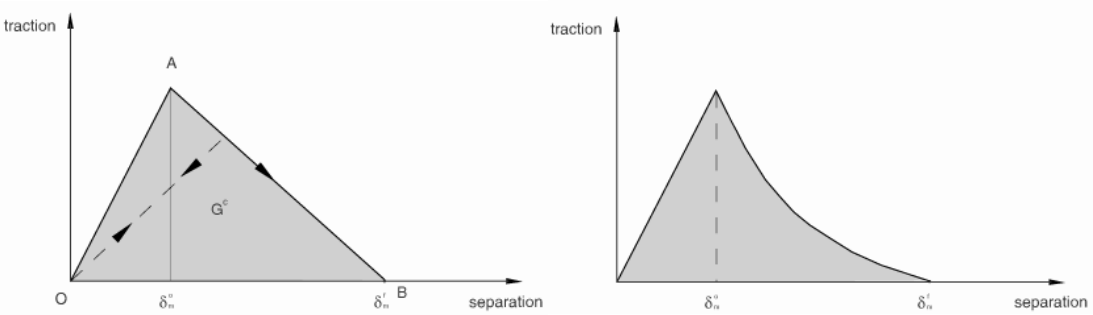

Figure 5.7: Linear and exponential damage evolution laws.

The value of the damage variable progresses from 0 to 1, with value 0 indicating the undamaged state and the value 1 indicating the fully damaged state.

Cohesive elements

There are two approaches regarding the modeling of cohesive elements in Abaqus. Cohesive elements can be embedded in an existing 3D mesh, thus sharing the same nodes as the adjacent elements. The other approach is the cohesive layer to be created as a different part and then be connected to the requested components using surface-based tie constraints. In the former approach, cohesive layer needs to have the exact same mesh as the neighboring components, whereas in the latter approach, different size of mesh can be used for the cohesive layer (usually finer).

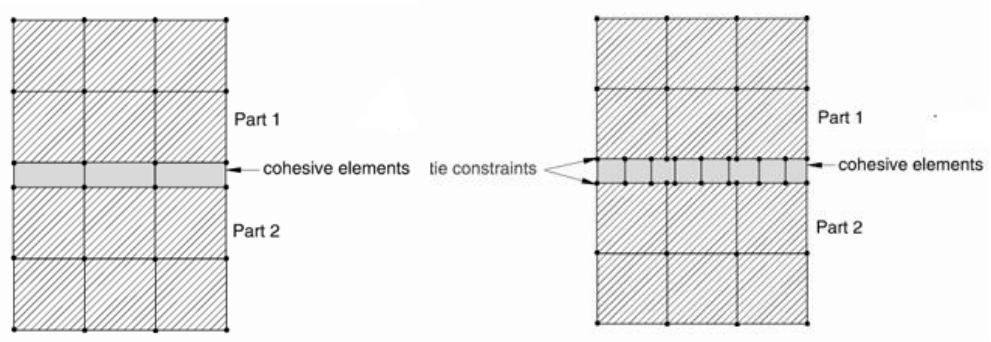

Figure 5.8: CZM modeling approaches

5.2.3. Introduction of CZM in the model

Cohesive elements where introduced in the skin-core interface of the model, following the second approach mentioned above. A new part was created for the cohesive layer of both interfaces of the specimen (top skin- core interface and bottom skin-core interface), of three-dimensional, deformable, solid type. The length and width of the layer created was equal to the ones of the specimen (600 mm length and 49.84 mm width), while the thickness of the layer was set to 0.05 mm.

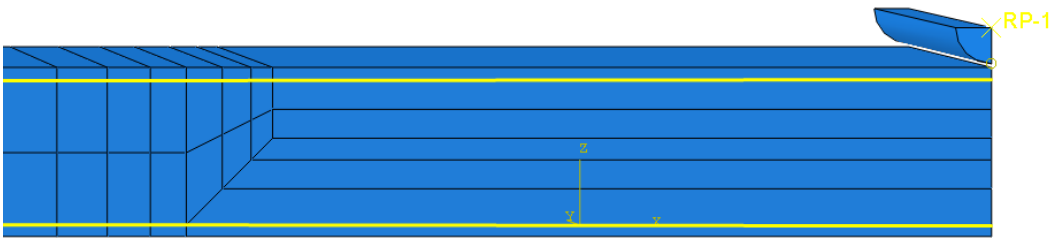

Figure 5.9: Introduction of cohesive elements in the interface between skins and core

Material orientation was assigned on the layer, with stacking direction the element isoparametric direction 3 (bottom to top).

A new section of type cohesive was created, with the cohesive zone material, the properties of which are mentioned further below, and the Traction Separation response and was then assigned to the cohesive layer.

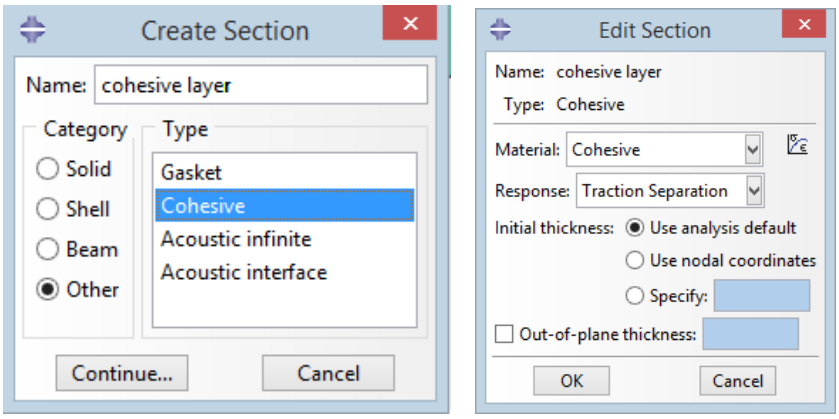

Figure 5.10: Creation of cohesive section with traction separation response

In the assembly module, two new instances of the cohesive layer part were created for the two interfaces and they were placed between the top skin and the core and between the bottom skin and the core, by adjusting their positions accordingly.

In the interaction module, the two cohesive layers were bonded to the neighboring components using surface-based tie constraints (two tie constraints per cohesive layer). In the tie constraints, as master surface was selected the relevant surface of the skin or core and as slave surface was selected the surface of the cohesive layer. In addition, in order to ensure that there would be no penetration between the skin and core in case of complete degradation of the cohesive elements, surface-to-surface contact was introduced between the two surfaces bonded by the cohesive layer.

With respect to the cohesive material, its elastic response was modeled as uncoupled traction (type traction) for which the parameters Enn, Ess and Ett had to be defined. As a damage initiation criterion was selected the quadratic nominal stress criterion and the damage evolution was defined as of energy type, with linear softening and a mixed mode behavior based on the Power Law. The value of parameter ***a*** in the power law was set to 1.2. For the damage initiation and evolution, the material properties that had to be defined were the three maximum nominal stress tn, tt and ts, as well as the three critical fracture energies G_n^C , G_s^C and G_t^C.

Looking through literature, various different values where found for the requested parameters, however, the exact values of the parameters for an interface between glass-polyester skin and PVC

foam core could not be obtained. Due to that the average values for the parameters were calculated based on the values found and a sensitivity analysis took place, modifying each time the value of one of the parameters and checking if there was an important difference in the results.

Table 5.1 Cohesive properties of the skin-core interface

Enn (GPa)	Ess - Ett (Gpa)	tn (MPa)	ts (MPa)	tt (MPa)	Gn (kJ/m2)	Gs - Gt (kJ/m2)
		25.10	50.00	50.00	0.300	0.800
2.400	0.857	20.00	40.00		0.643	0.905
3.000	0.896		36.50	27.60		
0.115	0.060					
1.850	0.560	21.63	17.90		0.430	4.700
		3.30	2.97		0.500	
2.400	1.000	50.00	45.00			
		80.00	100.00		0.969	1.719
		20.00	20.00			
		3.90			0.774	
		1.00	1.30		0.010	0.100
		3.30	3.30		0.490	0.380
					0.300	0.600
3.550	1.350	55.00	50.00			
		10.00	20.00	20.00	0.400	0.500
Average values						
2.156	0.787	24.436	32.248	32.533	0.482	1.213

The mesh of the cohesive layers was constructed by cohesive, linear, hexagonal elements of type COH3D8. A mesh of higher density in comparison to the adjacent parts, was created for the cohesive layers with elements' global size of 1 mm.

A sensitivity analysis of the cohesive layer properties was conducted by modifying each time one of the properties and checking what was the effect in the results.

The results that were obtained had very small variations for the different values of properties used.

For all the different values of cohesive properties that were tried, there was no damage in the cohesive elements, thus the shear stress-displacement results obtained, were almost identical to the results after skin damage & core material modeling.

The results obtained were only for the case in which non-linear geometries were not considered, since solutions could not converge with the option nlgeom enabled.

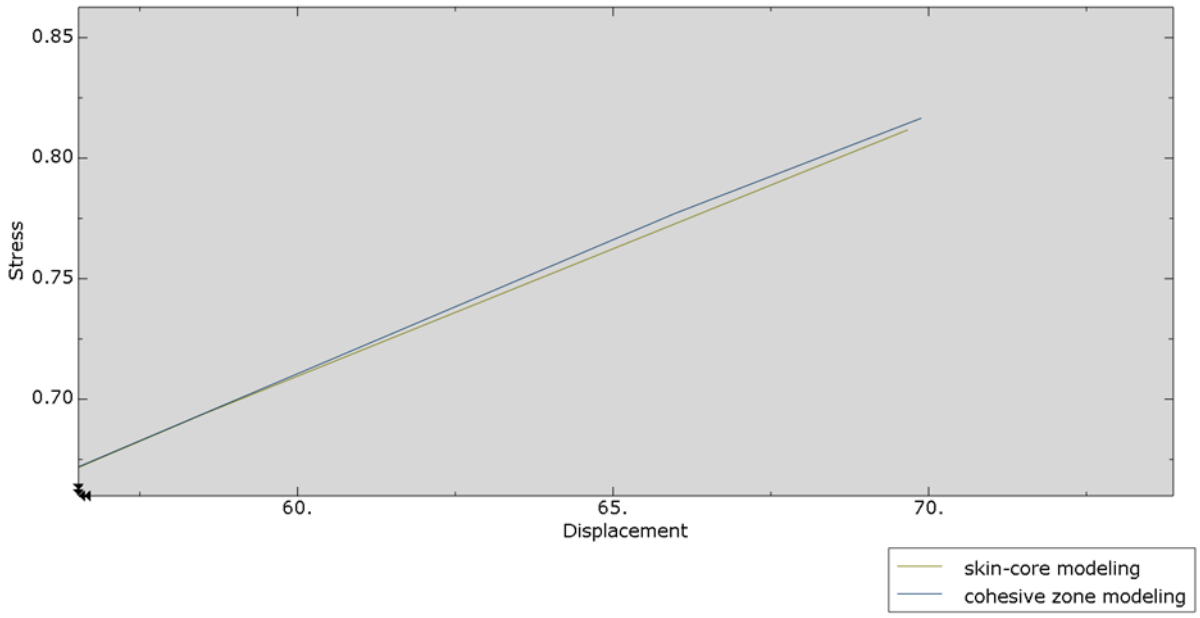

Figure 5.11: Shear stress-displacements curves for skin-core modeling and cohesive zone modeling

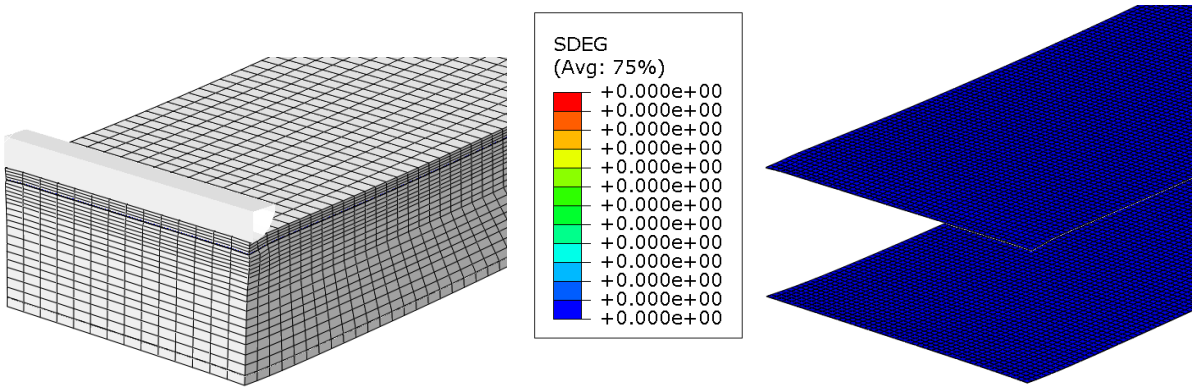

Figure 5.12: Damage variable of cohesive elements

6. Modeling the complete geometry of the 3-point bending test

Although in general the 3-point bending test can be considered a symmetrical problem, non-symmetries may be present, resulting in a non-symmetrical loading of the specimen. In addition, as observed from the 3-point bending test, the core of the specimen that has failed due to shear, seems to have broken on a plane next to the region that comes in contact with the loading part. The consideration of symmetry boundary conditions next to the region where the fracture has occurred may prevent the specimen from failing in such mode. Taking the above into consideration, a complete model of the 3-point bending test was created and cohesive zone modeling was introduced in the problem by inserting a cohesive layer through the thickness of the core in a 45°degrees plane, similar to the one depicted in the photo of the fractured specimen, trying this way to model the failure mode of the tested specimen.

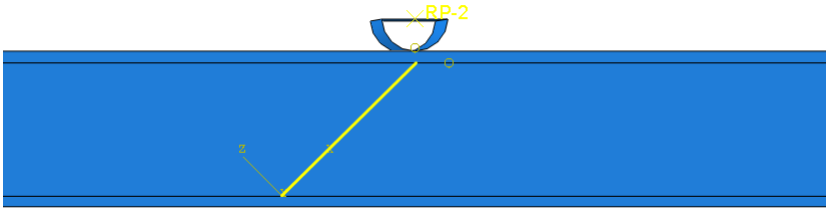

Figure 6.1 Introduction of cohesive elements through the core thickness

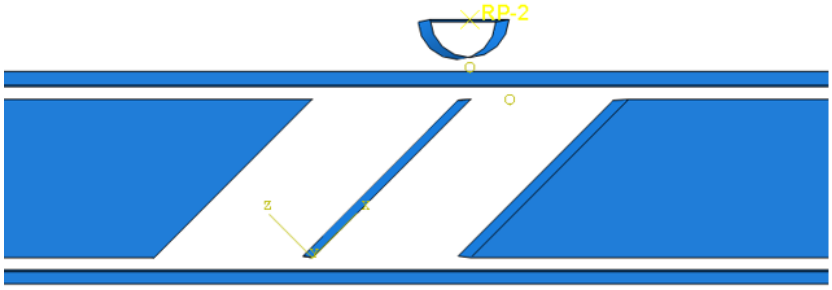

Figure 6.2 View of the parts unassembled.

The core was modeled as two parts which were connected with the cohesive layer, of 0.05 mm thickness, using tie constraints. The properties of the materials and the type of elements used in each part were defined the same as in the previous chapters.

With regard to the cohesive properties of the core, due to lack numerical of data for the PVC foam, the maximum stresses and fracture energies of PU foams, obtained through literature, where used instead.

The only property that could be found for a PVC foam material was the fracture energy in the normal direction G_n. The values of E_{nn}, E_{ss} and E_{tt} where defined the same as the ones of the modeled core.

Table 6.1 Cohesive properties of core

tn (MPa)	ts (Mpa)	tt (Mpa)	Gn (kJ/m2)	Gs (kJ/m2)	Gt (kJ/m2)
2.5	1.5	1.5	0.186	0.67	0.67

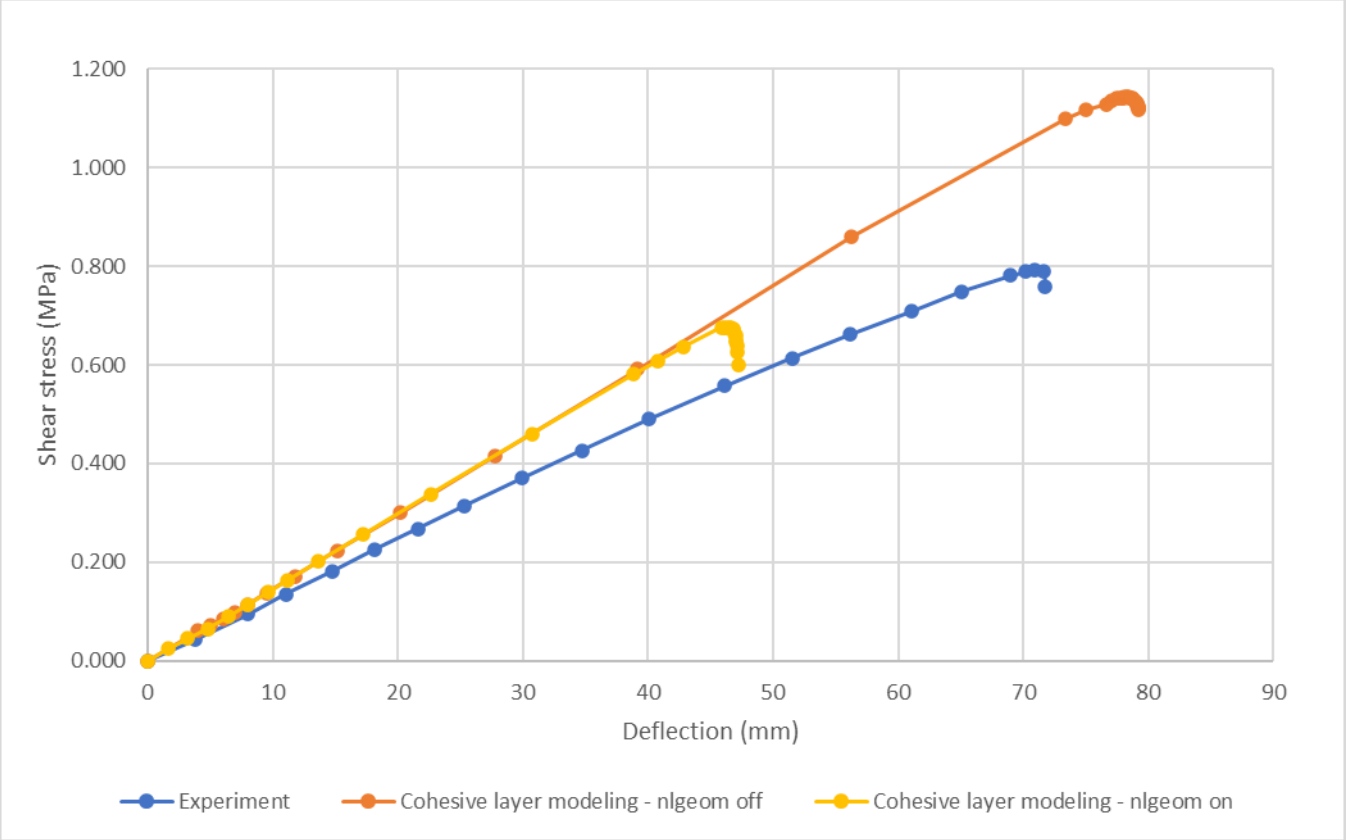

Figure 6.3 Shear stress-displacement curve

As can be observed in the above resulting curves, the introduction of the cohesive layer in the core, results in larger values of imposed force for the same displacement, or correspondingly, in smaller deflections of the specimen for the same value of the imposed force. This response of the specimen is probably observed due the fact that the cohesive properties that were used for the core are not the most

accurate and also because a small damping factor (1e-05) was used in order for the solution to be able to converge.

It is also observed that when non-linearities in geometry are being considered, the specimen fails at lower values of imposed force-deflection, whereas when non-linearities are not taken into account, the specimen seems to be able to withstand higher loads, in comparison to the tested specimen. In both cases it is observed that there is a significant amount of yield in the core and that skin damage is only present in the top skin.

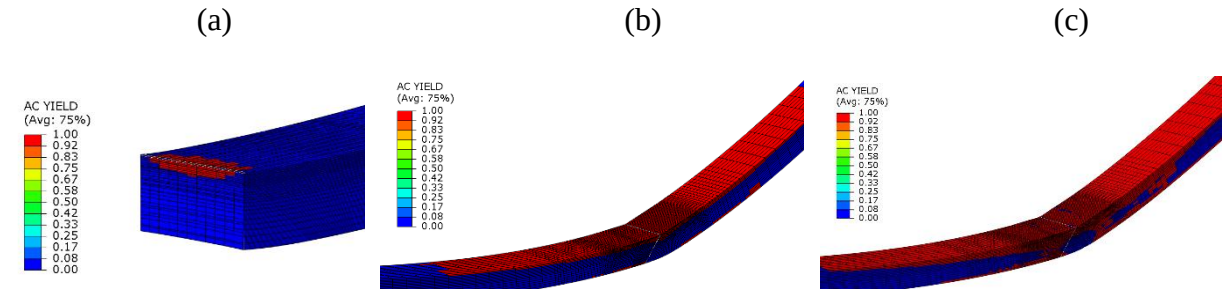

Figure 6.4 Core yield at (a) 55mm (b)73 and (c) maximum deflection (nlgeom-off)

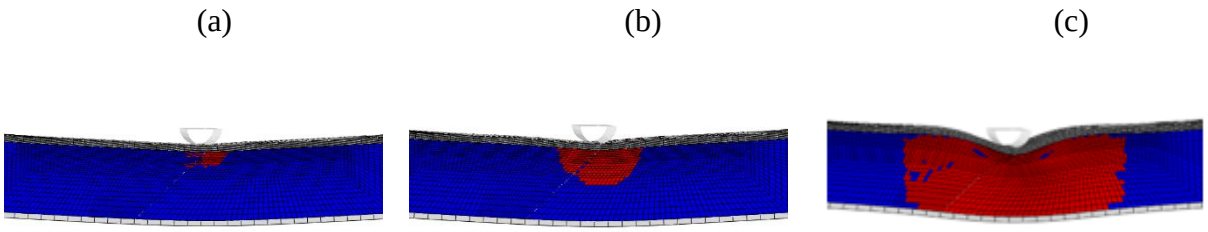

Figure 6.5 Core yield at (a) 40mm (b)45 and (c) maximum deflection (nlgeom-on)

With the non-linear geometric effects taken into account, damage is initiated in all plies of the top skin due to both matrix and fiber failure.

(a) (b) (c)

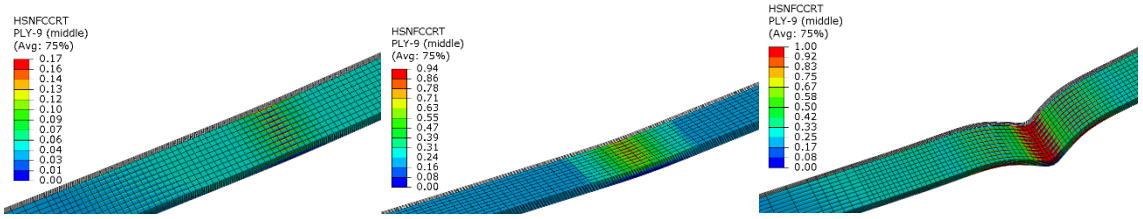

Figure 6.6 Damage evolution of ply-9 of top skin at (a) 15mm (b) 35mm (c) maximum deflection

(a) (b) (c)

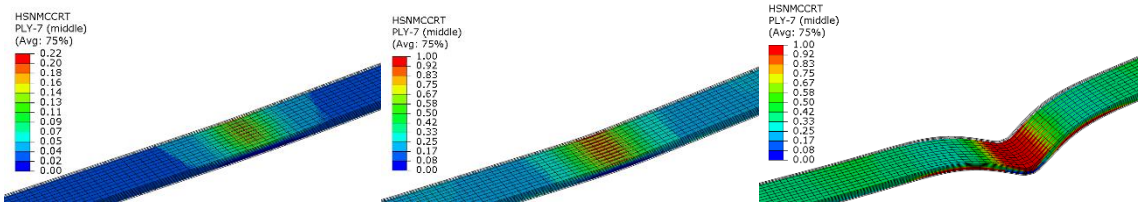

Figure 6.7 Damage evolution of ply-7 of top skin at (a) 15mm (b) 35mm (c) maximum deflection

With the non-linear geometric effects not taken into account, damage has again been initiated on all the plies of the top skin under the below mentioned modes of failure.

- in plies 4,8,9 due to fiber failure in compression
- in plies 2,5,6,7 due to matrix failure in compression
- in plies 1,3 due to a combination of fiber and matrix failure.

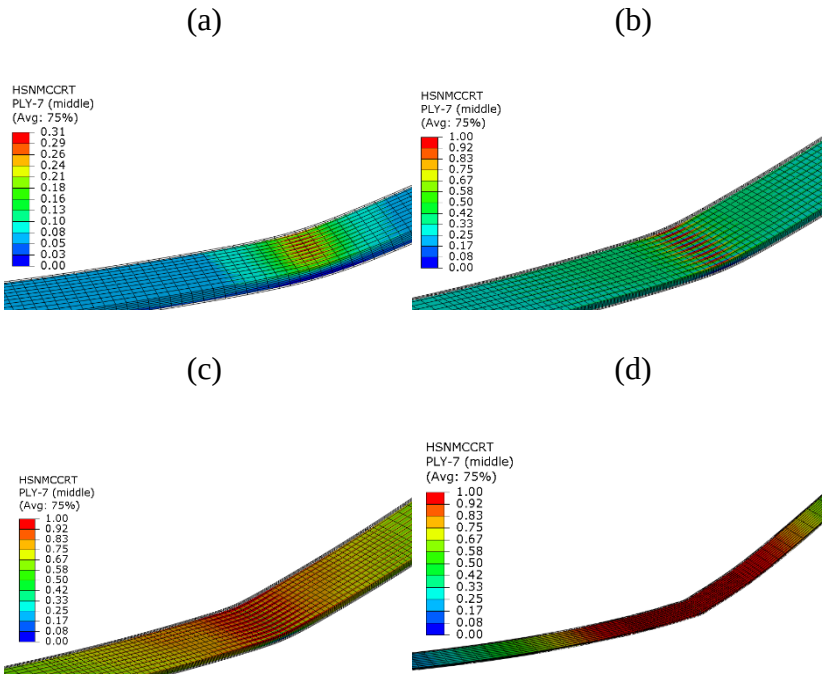

Figure 6.8 Damage evolution of ply-7 of top skin at (a) 20 (b) 40 (c) 60 and (d) maximum deflection

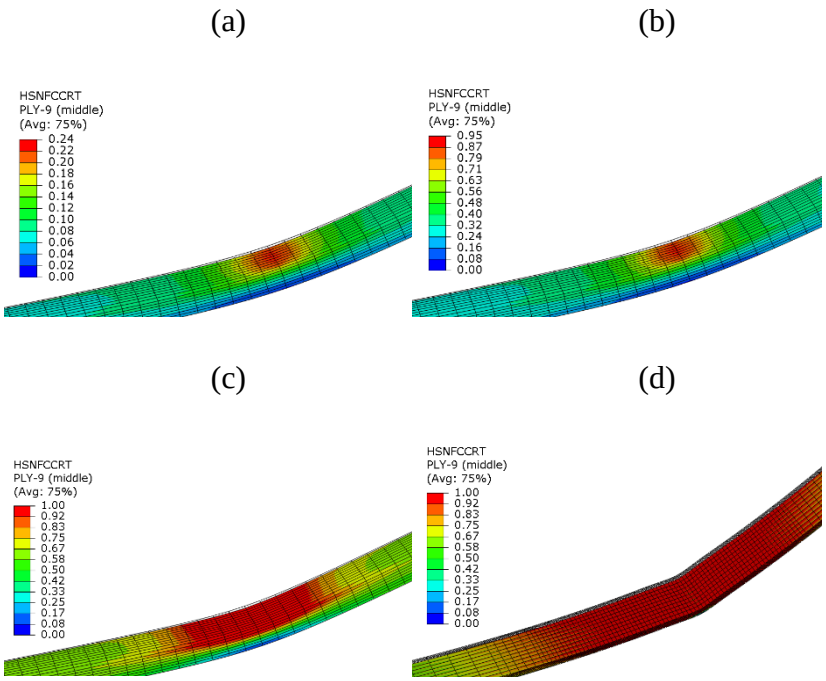

Figure 6.9 Damage evolution of ply-9 of top skin at (a) 20mm (b) 40mm (c) 60mm and (d) maximum deflection

In both cases, no initiation of damage has been observed in the cohesive layer in the core, since the value of the damage variable of all cohesive elements is smaller that 1.

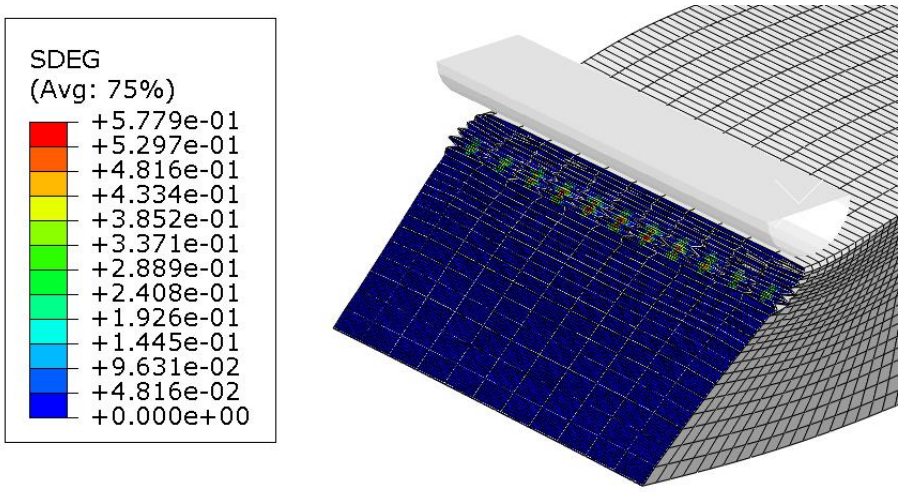

Figure 6.10 Damage variable of the cohesive elements

Since the values of the fracture energies due to damage in the normal and shear directions, that were used were approximate values found in literature, a sensitivity analysis on these values took place in order to investigate if there was any difference in the results. By altering the values of the fracture energies from -50% to +100% of the values shown in table 6.1, it was observed that there was a minor difference in the results.

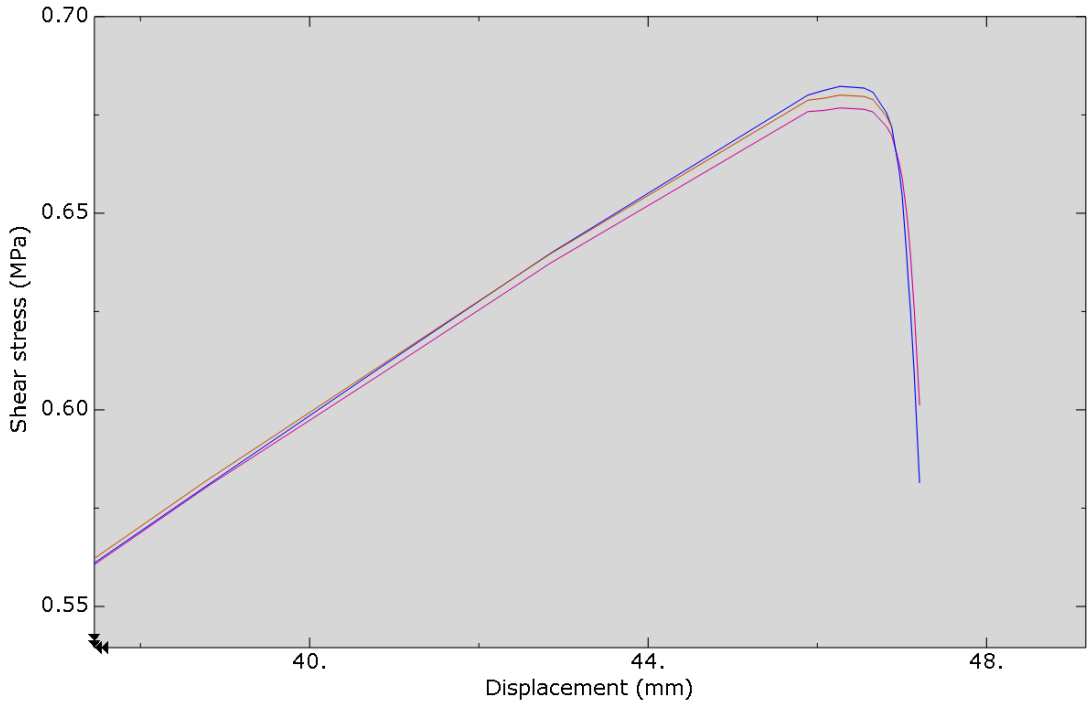

Figure 6.11 Shear stress – deflection curves for different values of the fracture energies

However, what seems to have an impact on the results, is the longitudinal position of the cohesive layer, since by moving the cohesive layer along the x-axis, towards the center of the specimen, a decrease in the maximum shear-stress/deflection was observed.

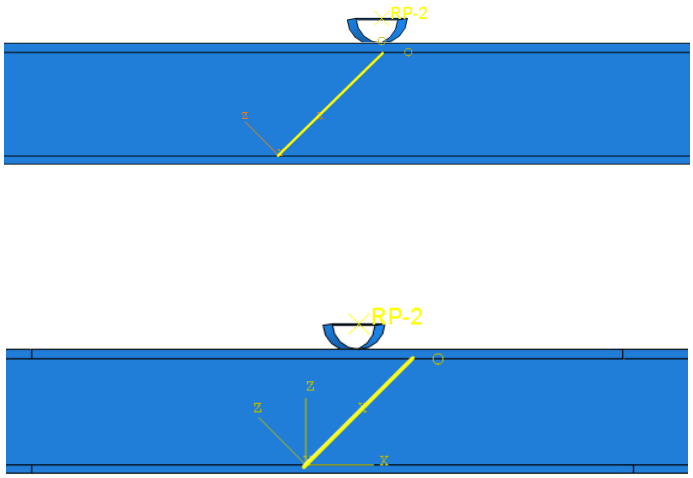

Figure 6.12 Different positions of the cohesive layer, top: position 1, bottom: position:2

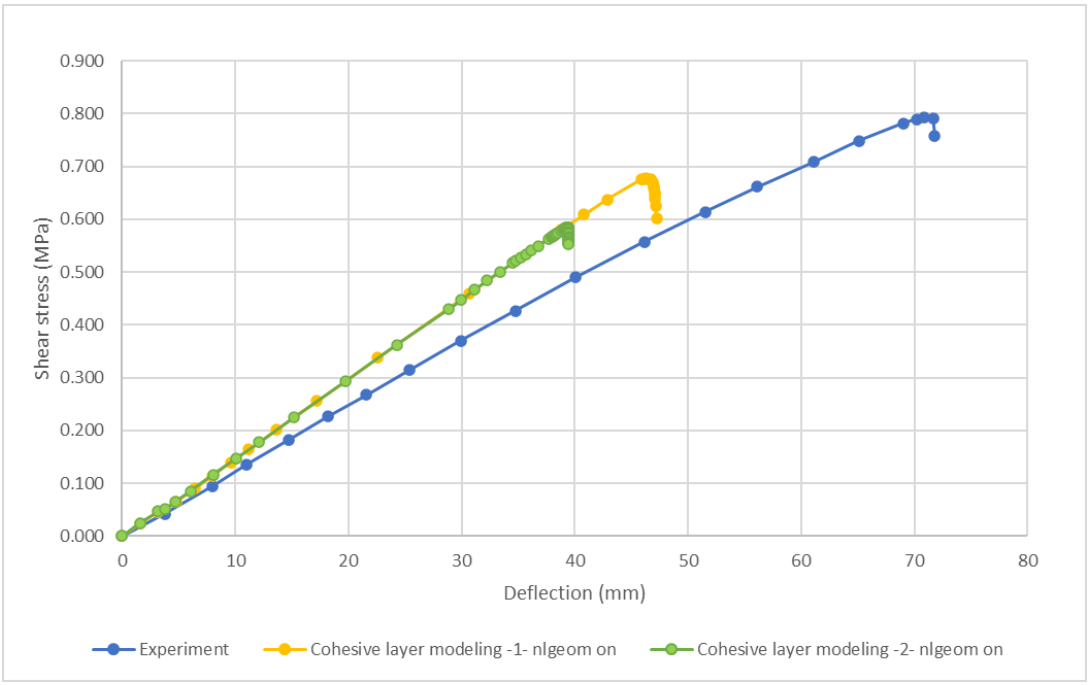

Figure 6.13 Shear stress – deflection curves for different positions of the cohesive layer

Although the damage of the skins was similar in the two cases, the important difference was in the level of plasticity in the core. In the first case there was significant plasticity in the core, while in the second case, core plasticity was observed only in a small region below the loading part.

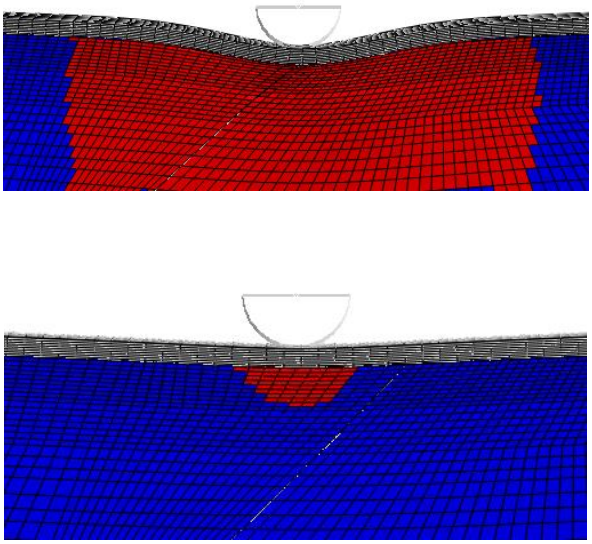

Figure 6.14 Shear stress – deflection curves for different positions of the cohesive layer

7. Conclusions

Tests on sandwich specimens were conducted by BV for the characterization of the core in shear, based on the testing standards ISO 14125 and ASTM C273. The aim was to see which one of those tests should be preferred for finding the shear properties of sandwich cores.

In this thesis, above tests were modeled using Finite Element Analysis, in order to investigate which are the failure mechanisms that occur. For the ISO 14125, half geometry of the problem was modeled, damage properties were inserted in the material of the skins and then a proper material model was created for the core, by modeling the ASTM C273 and creating a material that best fits the experimental results.

The modeling of the 3-point bending test, with only half-geometry, showed that the sandwich material softening during the apply of the load, is mainly due to the damage observed in the two skins, rather than the plasticity of the core, which is negligible.

Although the shape of the stress-displacement curve produced with this model, was in tune with the experimental results, the half-geometry model was able to withstand higher loads prior failure, adversely to the tested specimen which failed at a lower load.

In order to bring the model's response closer to the one observed during the experiment, pre-cracks and cohesive elements were introduced in the interface between the skins and the core, trying this way to model a possible debonding. The cohesive element modeling did not have an important effect on the specimen's response, however, the insertion of pre cracks had as a result the specimen being able to withstand lower values of imposed displacement.

In an effort to lead the model to a response similar to the one observed in the test, the complete model of the 3-point bending test was generated and cohesive elements were inserted through the thickness of the core, creating this way a path at which the specimen could brake due to shear. This had as a result, a great amount of yield on the core and damage initiation of all the plies of the top skin, while no damage initiation occurred in the bottom skin. The specimen modeled using the option of nlgeom, failed at lower values of imposed force-displacement in comparison to the actual tested specimen, while the specimen modeled without the option nlgeom was able to withstand higher values of imposed force. In addition, it was observed that the position of the 45˚ plane of cohesive elements affects the response of the specimen.

Both the complete model with a cohesive zone in core and the half-geometry model showed that there is severe damage on the top skin of the specimen and that damage occurs in all of the plies. In addition, the former, when used with non-linear geometric effects being considered, it showed a very large local deformation of the top skin below the loading part. This could lead to a crack be initiated in the interface of the top skin and core which could then kink into the core and cause the specimen to show a failure response same as the one in the experiment.

8. Recommendations for future work

The modeling that was followed captured well the form of softening of the shear-stress curve, however, it could not predict the exact point of failure. This can be more accurately predicted by having the exact elastic properties of the skins and core, as well as the damage properties of the skins and by obtaining through experiments the cohesive properties of the interface between the core and the skins and the cohesive response of the core itself. If these properties could be known, further modeling could be performed in order to validate the results obtained so far.

In addition to the modeling enhancement, more tests should be conducted on these sandwich specimens using the ISO 14125 standard, since the results obtained from the testing of only one specimen may not be the most accurate ones.

A way that could help to increase the effectiveness of the 3-point bending test, by means of increasing the possibilities of a specimen to break in shear, would be to perform a parametric analysis on the dimensions of the specimens, in order to figure out when a specimen is more likely to break due to shear. In this way, the dimensions of the tested specimens could be selected accordingly, so as for the specimens to break in the desirable failure mode.

9. References

[1] Ramesha Talreja, Janis Varna (2015), *Modeling Damage,Fatigue and Failure of Composite Materials,* Woodhead Publishing Series in Composites Science and Engineering

[2] P.K. Mallick (2010), *6 - Thermoset–matrix composites for lightweight automotive structures*, In Woodhead Publishing Series in Composites Science and Engineering, Materials, Design and Manufacturing for Lightweight Vehicles, Woodhead Publishing.

[3] Mohan M. Ratwani (2010), *Composite Materials and Sandwich Structures – A Primer.*

[4] A.P. Mouritz, E. Gellert, P. Burchill, K. Challis (2001), *Review of advanced composite structures for naval ships and submarines,* Composite Structures 53 (2001) 21-41.

[5] António Bastos Pereira, Fábio A.O. Fernandes (2019), *Sandwich Panels Bond with Advanced Adhesive Films,* Journal of Composite Science.

[6] Craig A. Steeves, Norman A. Fleck (2004), *Collapse mechanisms of sandwich beams with composite faces and a foam core, loaded in three-point bending. Part II: experimental investigation and numerical modelling,* International Journal of mechanical Sciences.

[7] Lucie MOLINA et Anaëlle VERVOITTE, *Simulation of sandwich panel specimens according to ISO 14125 and ASTM C273 standards and comparison with test results,* ECOLE CENTRALE DE NANTES

[8] M.H. Khan , K.T. Tan (2020), *Post-impact flexural collapse modes of composite sandwich structures in Arctic conditions: Analytical prediction and experimental validation,* Elsevier Ltd.

[9] J.L. ABOT, I.M. DANIEL AND E.E. GDOUTOS (2002), *Contact Law for Composite Sandwich Beams,* Journal of SANDWICH STRUCTURES AND MATERIALS Sage Publications

[10] Ali A Saeid and Steven L Donaldson (2016), Experimental and finite element evaluations of debonding in composite sandwich structure with core thickness variations, Advances in Mechanical Engineering Vol 8(9) 1-18, Sage Publications

[11] SIMULIA, ABAQUS/CAE USER'S GUIDE

[12] C. BERGGREEN, B. C. SIMONSEN, K. K. BORUM (2007), *Experimental and Numerical Study of Interface Crack Propagation in Foam-cored Sandwich Beams,* Journal of COMPOSITE MATERIALS, Vol. 41, No. 4/2007, Sage Publications.

[13] Ramesha Talreja and Chandra Veer Singh (2012), *Damage and Failure of Composite Materials,* Cambridge University Press.

[14] Christian Lundsgaard-Larsen, Christian Berggreen, Leif A. Carlsson (2010), *Tailoring Sandwich Face/Core Interfaces for Improved Damage Tolerance—Part I: Finite Element Analysis,* Springer

[15] G. Bragagnolo, A.D. Crocombe, S.L. Ogina, I. Mohagheghian , A. Sordon , G.Meeksb, C. Santoni (2020), *Investigation of skin-core debonding in sandwich structures with foam cores,* Elsevier Ltd.

[16] Pedro P. Camanho, Stephen R. Hallet, *Numerical modeling approaches to interlaminar failure of advanced composite materials,* Woodhead Publishing Series in Composites Science and Engineering

[17] Daniel W. Spring, Glaucio H. Paulino, *A growing library of three-dimensional cohesive elements for use in ABAQUS.*

[18] Yue Liu, Bernd Zwingmann, Mike Schlaich (2014), *Nonlinear Progressive Damage Analysis of Notched or Bolted Fibre-Reinforced Polymer (FRP) Laminates Based on a Three-Dimensional Strain Failure Criterion,* Polymers

[19] L. Daudeville, O. Allix, P. Ladeveze (1995), *Delamination analysis by damage mechanisms: Some applications,* Composites Engineering Vol. 5 No.1 17-24

[20] N. Tsouvalis (1998), A*nalysis and design of vessels from composite materials,* NTUA

[21] Oludare E. Oluwabusi and Elias A. Toubia, *In-Plane Shear Characterization of Composite GFRP-Foam Sandwich Panels,* J. Compos. Constr., 2019 ASCE

[22] Mohammad Heidari-Rarani, Mousa Sayedain (2019), *Finite element modeling strategies for 2D and 3D delamination propagation in composite DCB specimens using VCCT, CZM and XFEM approaches,* Elsevier Ltd.

[23] M. Soroush, K. Malekzadeh Fard, M. Shahravi (2018), *Finite Element Simulation of Interlaminar and Intralaminar Damage in Laminated Composite Plates Subjected to Impact,* Latin American Journal of Solids and Structures

[24] GILMER M. VIANA AND LEIF A. CARLSSON (2020), *Mechanical Properties and Fracture Characterization of Cross-Linked PVC Foams,* Journal of SANDWICH STRUCTURES AND MATERIALS, Vol. 4 Sage Publications

[25] E.J. Barbero, F.A. Cosso, R. Roman, T.L. Weadon (2012), *Determination of material parameters for Abaqus progressive damage analysis of E-glass epoxy laminates,* Elsevier Ltd.

[26] Isaac M. Daniel (2009), *Influence of Core properties on the failure of composite sandwich beams,* Journal of Mechanics of Materials and structures Volume 4, Mathematical sciences publishers.

[27] Umut Caliskan and M. Kemal Apalak (2019), *Low speed impact behavior of adhesively bonded foam-core sandwich T-joints,* Journal of Adhesion Science and Technology, 33:3, 217-242

[28] Laszlo P. Kollar and George S. Springer (2003), *Mechanics of Composite Structures,* Cambridge University Press.

[29] Nailong Zhao, Weizhe Wang, Yingzheng Liu (2018), *Intergranular mechanical behavior in a blade groove-like component by crystal plasticity model with cohesive zone model,* Engineering Fracture Mechanics, Elsevier Ltd.

[30] Christian Lundsgaard-Larsen, Christian Berggreen, Leif A. Carlsson (2010), Tailoring Sandwich Face/Core Interfaces for Improved Damage Tolerance—Part II: Experiments, Springer.

[31] C.T. Sun, Z.-H. Jin (2012), *Chapter 9 - Cohesive Zone Model, Fracture Mechanics,* Academic Press, Pages 227-246

[32] Busra Bartan Kumbasar (2016), *Progressive Interlaminar Failure Analysis In Composite Missile Structures,* Thesis, Graduate School of Natural and Applied Sciences of Middle East Technical Univeristy.

[33] Haixia Mei, Shravan Gowrishankar, Kenneth M. Liechti, Rui Huang (2010) *Initiation and propagation of interfacial delamination in integrated thin-film structures,* 2010 12th IEEE Intersociety Conference on Thermal and Thermomechanical Phenomena in Electronic Systems.

[34] Daniel Höwer, Bradley A. Lerch, Brett A. Bednarcyk, Evan J. Pineda, Stefanie Reese, Jaan-Willem Simon (2018), *Cohesive zone modeling for mode I facesheet to core delamination of sandwich panels accounting for fiber bridging,* Composite Structures,Volume 183, Pages 568-581

[35] Hossein Malekinejad Bahabadi, Amin Farrokhabadi, Gholam Hossein Rahimi (2020), *Investigation of debonding growth between composite skins and corrugated foam-composite core in sandwich panels under bending loading,* Engineering Fracture Mechanics,Volume 230.

[36] Lucas Amaro de Oliveira, Maurício Vicente Donadon, *Delamination analysis using cohesive zone model: A discussion on traction-separation law and mixed-mode criteria*, Engineering Fracture Mechanics, Volume 228.

[37] Mansourinik, Mohsen & Taheri-Behrooz, Fathollah. (2018), *The effect of interface debonding on flexural behaviour of composite sandwich beams,* Journal of Sandwich Structures & Materials 2020, Vol. 22(4) 1132–1156.

[38] Wouter Weijermars (2016), *Mechanical behaviour of composite sandwich panels in bending after impact,* Thesis, University of Twente.

[39] *ISO 14125: Fibre-reinforced plastic composites — Determination of flexural properties,* International Organization for Standardization (1998)

[40] Dassault Systèmes, *Getting Started with Abaqus: Interactive Edition:*

http://dsk-016-1.fsid.cvut.cz:2080/v6.12/books/gsa/default.htm?startat=ch08s07.html